ACCEPTED FOR PUBLICATION IN APJ
Preprint typeset using LATEX style emulateapj v. 08/22/09

arXiv:1402.1168v2 [astro-ph.CO] 1 May 2014

WHAT IS THE PHYSICAL ORIGIN OF STRONG LYα EMISSION? II. GAS KINEMATICS AND DISTRIBUTION OF LYα EMITTERS ‡

TAKATOSHI SHIBUYA[1,2], MASAMI OUCHI[1,3], KIMIHIKO NAKAJIMA[3,4], TAKUYA HASHIMOTO[3], YOSHIAKI ONO[1,3], MICHAEL RAUCH[5], JEAN-RENE GAUTHIER[6], KAZUHIRO SHIMASAKU[3,7], RYOSUKE GOTO[3], MASAO MORI[2], AND MASAYUKI UMEMURA[2].

accepted for publication in ApJ

ABSTRACT

We present a statistical study of velocities of Lyα, interstellar (IS) absorption, and nebular lines and gas covering fraction for Lyα emitters (LAEs) at $z \simeq 2$. We make a sample of 22 LAEs with a large Lyα equivalent width (EW) of $\gtrsim 50$ Å based on our deep Keck/LRIS observations, in conjunction with spectroscopic data from the Subaru/FMOS program and the literature. We estimate the average velocity offset of Lyα from a systemic redshift determined with nebular lines to be $\Delta v_{\rm Ly\alpha} = 234 \pm 9$ km s^{-1}. Using a Kolmogorv-Smirnov test, we confirm the previous claim of Hashimoto et al. (2013) that the average $\Delta v_{\rm Ly\alpha}$ of LAEs is smaller than that of LBGs. Our LRIS data successfully identify blue-shifted multiple IS absorption lines in the UV continua of four LAEs on an individual basis. The average velocity offset of IS absorption lines from a systemic redshift is $\Delta v_{\rm IS} = 204 \pm 27$ km s^{-1}, indicating LAE's gas outflow with a velocity comparable to typical LBGs. Thus, the ratio, $R_{\rm IS}^{\rm Ly\alpha} \equiv \Delta v_{\rm Ly\alpha}/\Delta v_{\rm IS}$ of LAEs, is around unity, suggestive of low impacts on Lyα transmission by resonant scattering of neutral hydrogen in the IS medium. We find an anti-correlation between Lyα EW and the covering fraction, f_c, estimated from the depth of absorption lines, where f_c is an indicator of average neutral hydrogen column density, $N_{\rm HI}$. The results of our study support the idea that $N_{\rm HI}$ is a key quantity determining Lyα emissivity.

Subject headings: cosmology: observations — early universe — galaxies: formation — galaxies: high-redshift

1. INTRODUCTION

Lyα Emitters (LAEs) are an important population of high-z star-forming galaxies in the context of galaxy formation. LAEs at $z = 2-7$ and beyond $z = 7$ are found by narrow-band (NB) imaging observations based on an NB excess resulting from their prominent Lyα emission (e.g., Cowie et al. 2010; Gronwall et al. 2007; Ciardullo et al. 2012; Ouchi et al. 2008; Ota et al. 2008; Ouchi et al. 2010; Hu et al. 2010; Finkelstein et al. 2007; Kashikawa et al. 2011, 2006; Shibuya et al. 2012). Observational studies on a morphology and spectral energy distribution (SED) of LAEs reveal that such a galaxy is typically young, compact, less-massive, less-dusty than other high-z galaxy populations, and a possible progenitor of Milky Way mass galaxies (e.g., Gronwall et al. 2011; Guaita et al. 2011; Ono et al. 2010; Gawiser et al. 2007; Dressler et al. 2011; Rauch et al. 2008; Dijkstra & Kramer 2012). Additionally, LAEs are used to measure the neutral hydrogen fraction at the reionizing epoch, because Lyα photons are absorbed by intergalactic medium (IGM).

Lyα emitting mechanism is not fully understood due to the highly-complex radiative transfer of Lyα in the interstellar medium (ISM). Many theoretical models have predicted that the neutral gas and/or dust distributions surrounding central ionizing sources are closely linked to the Lyα emissivity (e.g., Neufeld 1991; Finkelstein et al. 2008; Laursen et al. 2013, 2009; Laursen & Sommer-Larsen 2007; Duval et al. 2013; Zheng & Wallace 2013; Zheng et al. 2010; Yajima et al. 2012). Thus, resonant scattering in the neutral ISM can significantly attenuate the Lyα emission.

Lyα emissivity may not only depend on the spatial ISM distribution, but on the gas kinematics as well. The large-scale galactic outflows driven by starbursts or active galactic nuclei could allow Lyα photons to emerge at wavelengths where the Gunn-Peterson opacity is reduced, and consequently enhance the Lyα emissivity, particularly in the high-z Universe (e.g., Dijkstra & Wyithe 2010). The outflow may also blow out the Lyα absorbing ISM. The gas kinematics of LAEs has been evaluated from the Lyα velocity offset ($\Delta v_{\rm Ly\alpha}$) with respect to the systemic redshift ($z_{\rm sys}$) traced by nebular emission lines (e.g, Hα, [O III]) from their H II regions. In the past few years, deep NIR spectroscopic studies have detected nebular emission lines from ~ 10 LAEs at $z = 2-3$, and measured their $\Delta v_{\rm Ly\alpha}$ (McLinden et al. 2011; Hashimoto et al. 2013; Guaita et al. 2013; Finkelstein et al. 2011; Chonis et al. 2013). The Lyα emission lines for these LAEs are redshifted from their $z_{\rm sys}$ by a $\Delta v_{\rm Ly\alpha}$ of $200-300$ km s^{-1}.

Electronic address: shibyatk_at_icrr.u-tokyo.ac.jp
[1] Institute for Cosmic Ray Research, The University of Tokyo, 5-1-5 Kashiwanoha, Kashiwa, Chiba 277-8582, Japan
[2] Center for Computational Sciences, The University of Tsukuba, 1-1-1 Tennodai, Tsukuba, Ibaraki 305-8577 Japan
[3] Department of Astronomy, Graduate School of Science, The University of Tokyo, Tokyo 113-0033, Japan
[4] Institute for the Physics and Mathematics of the Universe (IPMU), TODIAS, The University of Tokyo, 5-1-5 Kashiwanoha, Kashiwa, Chiba 277-8583, Japan
[5] Observatories of the Carnegie Institution of Washington, 813 Santa Barbara Street, Pasadena, CA 91101, USA
[6] Cahill Center for Astronomy and Astrophysics, California Institute of Technology, MS 249-17, Pasadena, CA 91125, USA
[7] Research Center for the Early Universe, Graduate School of Science, The University of Tokyo, Tokyo 113-0033, Japan

‡ Based on data obtained with the Subaru Telescope operated by the National Astronomical Observatory of Japan.

Hashimoto et al. (2013) find an anti-correlation between Lyα equivalent width (EW) and $\Delta v_{\rm Ly\alpha}$ in a compilation of LAE and LBG samples. This result is in contrast to a simple picture where Lyα photons more easily escape in the presence of a galactic outflow.

However, the Lyα velocity offset is thought to increase with both resonant scattering in H I gas clouds as well as galactic outflow velocity (e.g., Verhamme et al. 2006, 2008). The anti-correlation could result from a difference in H I column density ($N_{\rm HI}$) rather than outflowing velocity. The gas kinematics can be investigated more directly from the velocity offset between interstellar (IS) absorption lines of the rest-frame UV continuum and $z_{\rm sys}$ (IS velocity offset; $\Delta v_{\rm IS}$). The IS velocity offset traces the speed of outflowing gas clouds, and may help to distinguish the two effects on $\Delta v_{\rm Ly\alpha}$.

For UV-continuum selected galaxies, the $\Delta v_{\rm IS}$ has been measured for $>$ 100 objects (e.g. Pettini et al. 2001; Christensen et al. 2012; Kulas et al. 2012; Schenker et al. 2013; Steidel et al. 2010). Steidel et al. (2010) find that LBGs have an average of $\langle \Delta v_{\rm IS} \rangle = -164$ km s^{-1} in their sample of 89 LBGs at $z \sim 3$. This statistical study indicates ubiquitousness of galactic outflow in LBGs. However, there have been no NB-selected galaxies with a $\Delta v_{\rm IS}$ measurement to date except for a stacked UV spectrum in Hashimoto et al. (2013). This is because it is difficult to estimate $\Delta v_{\rm IS}$ for individual LAEs, especially for galaxies with a large Lyα EW of $\gtrsim 50$ Å due to their faint UV-continuum emission, while $\Delta v_{\rm IS}$ are measured for some UV-selected galaxies with EW(Lyα) ~ 50 Å (e.g., Erb et al. 2010). A statistical investigation of Lyα kinematics for LAEs could shed light on the physical origin of the anti-correlation and the underlying Lyα emitting mechanism.

This is the second paper in the series exploring the Lyα emitting mechanisms[9]. In this paper, we present the results of our optical and NIR spectroscopy for a large sample of $z = 2.2$ LAEs with Keck/LRIS and Subaru/FMOS to verify possible differences of $\Delta v_{\rm Ly\alpha}$ and $\Delta v_{\rm IS}$ between LAEs and LBGs. These spectroscopic observations are in an extension of the project of Hashimoto et al. (2013) aiming to confirm the anti-correlation between Lyα EW and $\Delta v_{\rm Ly\alpha}$. The organization of this paper is as follows. In Section 2, we describe the details of the LAEs targeted for our spectroscopy. Next, we show our optical and NIR spectroscopic observations in Section 3. We present methods to reduce the spectra, and to measure kinematic quantities such as $\Delta v_{\rm Ly\alpha}$ and $\Delta v_{\rm IS}$ in 4. We perform SED fitting to derive physical properties in Section 5. We compare kinematic properties between LAEs and LBGs in Section 6, and discuss physical origins of possible differences in these quantities in Section 7. In the last section Section 8, we summarize our findings.

Throughout this paper, we adopt the concordance cosmology with $(\Omega_m, \Omega_\Lambda, h) = (0.3, 0.7, 0.7)$, (Komatsu et al. 2011). All magnitudes are given in the AB system (Oke & Gunn 1983).

2. TARGETS FOR SPECTROSCOPY

Our targets for optical and NIR spectroscopy are $z = 2.2$ LAEs selected by observations of the Subaru/Suprime-Cam (Miyazaki et al. 2002) equipped with the narrow-band (NB) filter, NB387 ($\lambda_c = 3870$ Å and FWHM = 94 Å) (Nakajima et al. 2012, 2013). The details of observations and selection for LAEs are given in these papers, but we provide a brief description as follows. The Suprime-Cam observations have been carried out for LAEs at $z = 2.2$ with NB387 in a total area of ~ 1.5 square degrees. Based on the color selection of $B - NB387$ and $u^* - NB387$, the Suprime-Cam observations have located 619, 919, 747, 950, and 168 LAEs in the Cosmic Evolution Survey (COSMOS) (Scoville et al. 2007), the Subaru/*XMM-Newton* Deep Survey (SXDS) (Furusawa et al. 2008), the Chandra Deep Field South (CDFS) (Giacconi et al. 2001), the *Hubble* Deep Field North (HDFN) (Giavalisco et al. 2004), and the SSA22 (e.g., Steidel et al. 2000) fields, respectively. In the above five fields, a total of ~ 3400 LAEs have been selected down to a Lyα EW of $20 - 30$ Å in rest-frame (Nakajima et al. in prep.). This large sample size enables us to study statistically various properties of high-z LAEs, such as structural properties (Shibuya et al. 2014) and the statistics of Lyα halos (Momose et al. 2014).

3. OBSERVATION

3.1. *Optical Spectroscopy for Lyα and UV Continuum Emission*

We have carried out optical spectroscopy for our $z = 2.2$ LAE sample with the Low Resolution Imaging Spectrometer (LRIS; Oke et al. 1995; Steidel et al. 2004) on the Keck I telescope in order to detect their redshifted Lyα emission lines. We used six multi-object slit (MOS) masks for LAEs selected in the NB387 imaging observations in the COSMOS, HDFN, HUDF, SSA22, and SXDS fields. The mask for the objects in the HUDF includes two LAEs whose nebular emission lines were detected in the 3D-*HST* survey (H. Atek et al. in preparation). The total number of LAEs observed with these LRIS masks is 83. The observations were conducted on March 19-21 and November 14-15, 2012 (UST) with seeing sizes of 0.″7-1.″6. Spectrophotometric standard stars were observed on each night for flux calibrations. The spectral resolution is $R \sim 1000$. The number of observed LAEs, grisms, central wavelength and observing time in each slit-masks are summarized in Table 1.

3.2. *Near-Infrared Spectroscopy for Nebular Emission*

To calculate systemic redshifts of our LAEs from their nebular emission lines, we use NIR spectroscopic data obtained from observations with the Fiber Multi Object Spectrograph (FMOS; Kimura et al. 2010) on the Subaru telescope on December 22, 23, and 24, 2012 (UST). All of LAEs in the SXDS and COSMOS fields are observed with J and H-band filters of FMOS. Details of the FMOS observation and reduction are shown in Nakajima et al. in prep. The systemic redshifts for objects were derived by simultaneously fitting to Hβ and [O III]λ4958, 5007 emission lines by using their vacuum wavelengths in rest-frame.

4. SPECTROSCOPIC DATA

4.1. *Reduction of LRIS Spectra*

[9] The first paper presents a study on LAE structures (Shibuya et al. 2014).

TABLE 1
Summary of the Keck/LRIS Observations

Slit Mask	$n_{\rm LAE}/n_{\rm obj}$	Grating/$\lambda_{\rm c}$ [Å]	t_1 [s]	$n_{\rm frame}$	$T_{\rm exp}$ [s]	Date of Observations
(1)	(2)	(3)	(4)	(5)	(6)	(7)
COSMOS	14/16	600/4000	3000	8	24000	2012 March 19-21
HDFN1	18/22	600/4000	3000	6	18000	2012 March 20
HDFN2	18/20	1200/3400	2800 − 3000	6	17800	2012 March 19-20
COSMOS3B	18/22	600/4000	3000	3	9000	2012 November 15
HUDF_maB	10/31	400/3400	2758 − 3000	2	5758	2012 November 14
SXDS495B	10/30	600/4000	2136 − 3000	14	40854	2012 November 14-15

Note. — Columns: (1) Slit mask. (2) Number of objects included in the slit mask. (3). Grating and the central wavelength. (4) Exposure time of one frame. (5) Number of exposure. (6) Exposure time. (7) Date of observations.

Our LRIS spectra in each MOS mask are reduced with the public Low-Redux (`XIDL`) pipeline[10], for longslit and multi-slit data from the spectrographs on the Keck, Gemini, MMT, and Lick telescopes. We reduce the spectra of LAEs with this software in the following manner. First, we create flats, calibrate wavelengths with the arc data, and reject sources illuminated by the cosmic ray injections for 2-D spectra in the MOS masks. Next, we automatically identify emission lines and continua, and trace them in each slit in individual one-frame masks. After the source identification, we subtract the sky background, and correct for the distortion of the 2-D MOS mask images using sky lines. According to the information on the source identifications, we extract 1-D spectra from each slit in individual mask images. Finally, we stack the extracted 1-D spectra.

The public `XIDL` software extracts 1-D spectra from each one-exposure frame *before* combining these 2-D mask images. This process makes it difficult to detect faint emission lines and continua that are undetectable in individual one-exposure images. Then, we additionally search for faint emission lines from stacked 2-D images by visual inspection *after* combining one-exposure frames.

In total, the Lyα emission lines are detected from 26 objects in the LRIS spectroscopy. Figure 1 shows the spectroscopic success rate in the detection of Lyα emission. The success rate is $\sim 70\%$ for bright objects with NB387$\lesssim 24.5$. However, low detection and/or selection completeness at NB387$\gtrsim 24.5$ reduces largely the success rate ($\sim 20\%$). The photometric and spectroscopic properties of these Lyα-detected objects are listed in Table 2. Among these LRIS spectra, we identify eight LAEs with detections of Lyα and nebular emission lines excluding AGN-like objects.

4.2. *Measurement of Lyα Velocity Offset*

We measure the Lyα velocity offset for the eight LAEs with detections of Lyα and nebular lines:

$$\Delta v_{\rm Ly\alpha} = c\frac{z_{\rm Ly\alpha} - z_{\rm sys}}{1 + z_{\rm sys}}, \qquad (1)$$

where c, $z_{\rm Ly\alpha}$, and $z_{\rm sys}$, are the speed of light, and Lyα and systemic redshifts, respectively. The systemic redshift is determined from nebular emission lines obtained with FMOS.

[10] http://www.ucolick.org/~xavier/LowRedux/

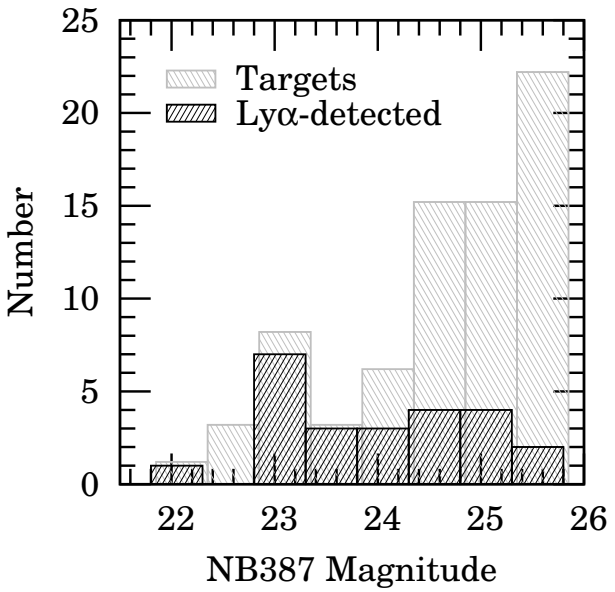

Fig. 1.— Success rate in identifying a Lyα emission line in the LRIS spectroscopy as a function of NB387 magnitude. The gray histogram shows the number of targeted LAEs. The black histogram indicate the number of LAEs with a Lyα detection. The histogram of targeted LAEs is slightly shifted for clarity.

Prior to the measurement of $\Delta v_{\rm Ly\alpha}$, we measure the wavelength of Lyα in the following line-fitting procedures. We use the peak wavelength of the best-fit asymmetric Gaussian profile for measurements of the Lyα wavelength. We first search automatically for an emission line in a wavelength range of $3500 - 4000$ Å in each spectrum. This range includes the wavelength range of the NB387 filter. Next, we fit an asymmetric Gaussian profile to the detected lines. The asymmetric Gaussian profile is expressed as

$$f(\lambda) = A\exp\left(\frac{-(\lambda - \lambda_0^{\rm asym})^2}{2\sigma_{\rm asym}^2}\right) + f_0, \qquad (2)$$

where A, λ_0, and f_0 are the amplitude, peak wavelength of the emission line, and continuum level, respectively. The asymmetric dispersion, $\sigma_{\rm asym}$, is represented by $\sigma_{\rm asym} = a_{\rm asym}(\lambda - \lambda_0^{\rm asym}) + d$, where $a_{\rm asym}$ and d are the asymmetric parameter and typical width of the line, respectively. An object with a positive (negative) $a_{\rm asym}$ value has a skewed line profile with a red (blue)

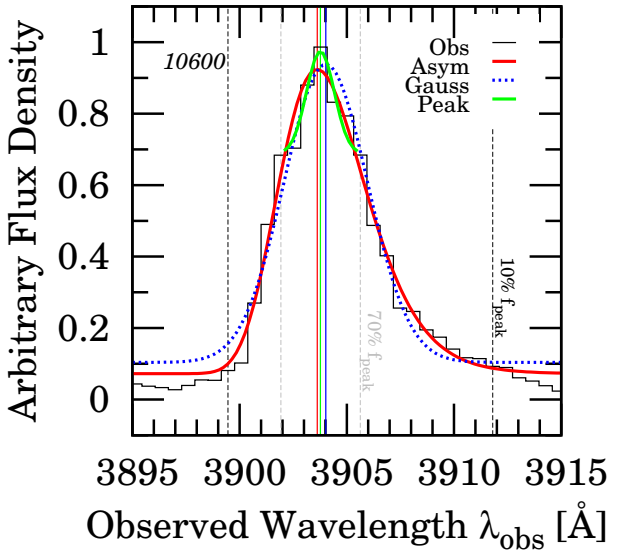

FIG. 2.— Observed Lyα emission line (black) for an example LAE, 10600, and its best-fit profiles. The curves are the best-fit symmetric Gaussian profiles in the wavelength range where the flux drops to 70 % (green) and 10 % (blue) of its peak, and the asymmetric Gaussian profile (red). The vertical bold lines denote the corresponding peak wavelengths of the best-fit profiles. The peak wavelengths are 3903.77, 3904.02, and 3903.62 Å, respectively, with the central, symmetric Gaussian, and asymmetric Gaussian profiles. The vertical dashed lines indicate the wavelengths where the flux drops to 70 % (gray) and 10 % (black) of its peak. See details in §4.2.

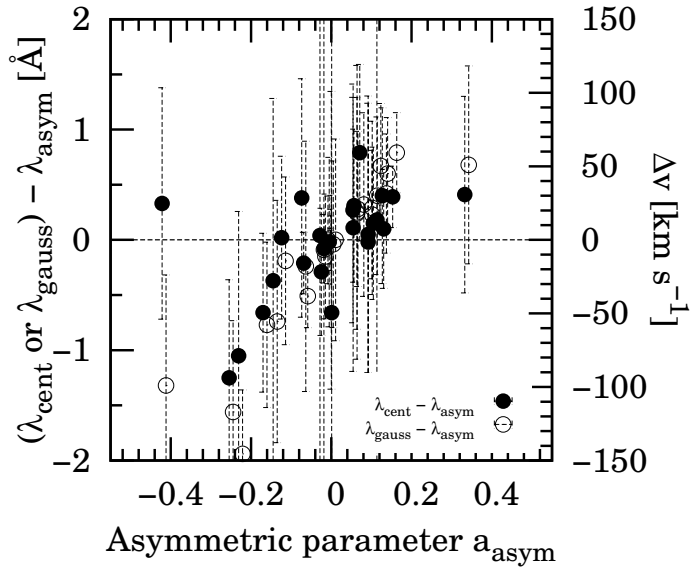

FIG. 3.— Differences between peak wavelengths of the best-fit central (filled circles) or symmetric Gaussian (open circles) profiles and ones of asymmetric Gaussian profile for Lyα-detected objects. Right vertical axis indicates the corresponding velocity offset. See details in Section 4.2.

wing. The fitting with the asymmetric Gaussian profile is efficient for Lyα line from high-z galaxies affected by complex kinematic structure of infalling and/or outflowing gas and IGM absorption. For fitting, we use data points over the wavelength range where the flux drops to 10% of its peak value at the redder and bluer sides of the emission line. We use the peak flux, wavelength of the line peak, 0.4, 1.0×10^{-17}, and 2.0 as the initial parameters of A, $\lambda_0^{\rm asym}$, $a_{\rm asym}$, f_0, and d for the line-fitting. The last two are typical values of our spectra. If profile fitting does not converge to the minimum in χ^2, we search for the best-fit by changing the initial value of $a_{\rm asym}$.

We show the best-fit asymmetric Gaussian profile for an example spectrum in Figure 2. We also fit a *symmetric* Gaussian profile to the emission lines in addition to asymmetric one. For the symmetric Gaussian fitting, we adopt two wavelength ranges where the flux drops to 70% and 10% of its peak value, and denote the corresponding peak wavelengths by $\lambda_0^{\rm gauss}$ and $\lambda_0^{\rm cent}$, respectively. The fitting procedure in the former narrow range is similar as in Hashimoto et al. (2013) in terms of avoiding systematic effects due to asymmetric line profile. As shown in Fig. 2, the best-fit $\lambda_0^{\rm asym}$ is broadly equal to $\lambda_0^{\rm cent}$ for the example line. The wavelength difference is $\sim+0.1$ Å($\sim+10$ km s^{-1} at $z=2.2$). In contrast, $\lambda_0^{\rm gauss}$ differs from $\lambda_0^{\rm asym}$ by $\sim+0.4$ Å which corresponds to a velocity difference of $\sim+30$ km s^{-1} at $z=2.2$. This is likely to be caused by the sharp drop on the blue side and the extended red tail which cannot be fit well with symmetric profiles.

This trend is more clearly shown in Figure 3 which exhibits the wavelength difference of $\lambda_0^{\rm gauss}$ and $\lambda_0^{\rm cent}$ from $\lambda_0^{\rm asym}$ as a function of the asymmetric parameter, $a_{\rm asym}$. The wavelengths of individual profiles are in good agreement for almost symmetric lines with $a_{\rm asym}\sim0$. Even for moderately-asymmetric profile with $|a_{\rm asym}|\lesssim0.2$, $\lambda_0^{\rm cent}$ tends to correct for systematic effects of skewed lines compared to $\lambda_0^{\rm gauss}$. However, both of $\lambda_0^{\rm gauss}$ and $\lambda_0^{\rm cent}$ are redshifted (blueshifted) from $\lambda_0^{\rm asym}$ by $\sim0.5-1.0$ Å for highly-asymmetric lines with $a_{\rm asym}\sim+0.4$ (-0.4).

After correcting for the heliocentric motion of Earth for the redshifts of Lyα and nebular lines[11], we calculate $\Delta v_{\rm Ly\alpha}$ following Equation 1. Table 2 lists the $z_{\rm Ly\alpha}$, $z_{\rm sys}$, and $\Delta v_{\rm Ly\alpha}$ for the 26 Lyα-detected objects observed with LRIS. Figure 4 present Lyα spectra as a function of velocity for LAEs with detections of nebular emission lines. In Table 3, we also list these quantities of the four LAEs with detections of Lyα and nebular lines obtained by previous Magellan/IMACS observations (Nakajima et al. 2012). Almost all objects observed with LRIS have a $\Delta v_{\rm Ly\alpha}$ of $\sim$ 200 km s^{-1} which is consistent with values in previous studies (e.g., Hashimoto et al. 2013). The values of $\Delta v_{\rm Ly\alpha}$ in the IMACS sample are calculated to be smaller than the LRIS results. This could be caused by large uncertainties due to the IMACS spectroscopy with a lower spectral resolution than LRIS.

Additionally, we provide a consistency check for our measurement of $z_{\rm Ly\alpha}$ by using the same object as in Hashimoto et al. (2013), COSMOS-13636. The object has been observed with both of LRIS in this work and Magellan/MagE in a previous work. The redshift of Lyα estimated from the LRIS spectrum ($z_{\rm Ly\alpha}^{\rm LRIS}=2.1626\pm0.00073$) is in good agreement with that of MagE ($z_{\rm Ly\alpha}^{\rm MagE}=2.16229\pm0.00008$) within a 1σ fitting error.

[11] http://fuse.pha.jhu.edu/support/tools/vlsr.html

TABLE 2
SUMMARY OF THE LYα-DETECTED OBJECTS IN THE LRIS SPECTROSCOPY

Slit Mask	Object	R.A.	Decl.	U	NB387	B	$\lambda_{\rm obs}$ [Å]	$z_{\rm Ly\alpha}$	$f(Ly\alpha)$ [10^{-17}erg/s/cm^2]	$L(Ly\alpha)$ [10^{42}erg/s]	EW(Lyα) [Å]	$z_{\rm sys}$	$\Delta v_{\rm Ly\alpha}$ [km s^{-1}]	$F_{\rm blue}/F_{\rm tot}$
(1)	(2)	(3)	(4)	(5)	(6)	(7)	(8)	(9)	(10)	(11)	(12)	(13)	(14)	(15)
COSMOS	12027	149.9343976	+2.1285326	24.2	23.4	24.5	3878.72 ± 0.24	2.1906	5.6 ± 0.3	2.0 ± 0.1	$73.69^{+6.91}_{-6.44}$	···	···	···
	12805[b]	150.0637013	+2.1354116	23.7	23.3	23.8	3843.27 ± 0.65	2.16144	7.4 ± 0.7	2.6 ± 0.3	$33.73^{+5.98}_{-5.52}$	2.15872	258 ± 51	0.24
	13138	150.0108585	+2.1401388	24.9	24.6	25.0	3866.73 ± 0.89	2.18074	1.2 ± 0.2	0.43 ± 0.07	$40.36^{+9.64}_{-8.44}$	2.17921	144 ± 69	0.40
	13636[bd]	149.9974498	+2.1439906	23.9	23.0	24.1	3844.68 ± 1.30	2.1626	9.6 ± 0.5	3.3 ± 0.2	$86.80^{+8.31}_{-7.76}$	2.16052	197 ± 102[f]	0.13
	14212[b]	149.9585714	+2.1482830	24.0	23.3	24.0	3879.99 ± 0.52	2.19165	6.7 ± 0.6	2.4 ± 0.2	$54.98^{+5.56}_{-5.18}$	2.18955	188 ± 40	0.23
	08357[a]	149.9961405	+2.0921070	24.8	24.4	24.9	3868.79 ± 0.86	2.18243	1.4 ± 0.4	0.50 ± 0.14	$46.68^{+8.60}_{-7.69}$	2.18044	205 ± 66	0.13
	13820[a]	149.9554179	+2.1470628	25.6	25.1	25.9	3820.20 ± 1.01	2.14246	2.1 ± 0.2	0.72 ± 0.07	$98.86^{+31.30}_{-26.40}$	···	···	···
	14135[a]	149.9770609	+2.1508410	27.0	25.9	26.8	3893.06 ± 1.08	2.2024	0.62 ± 0.1	2.3 ± 0.4	$100.02^{+30.70}_{-24.26}$	···	···	
HDFN1	18325[c]	189.0973399	+62.1014179	22.9	21.6	23.2	3858.78 ± 0.25	2.1742	30.0 ± 0.9	10.6 ± 0.3	$151.61^{+3.52}_{-3.45}$	···	···	···
	20042[a]	189.0293966	+62.1176510	25.4	24.7	25.6	3864.87 ± 2.12	2.17921	1.5 ± 0.4	0.53 ± 0.14	$108.42^{+12.48}_{-11.36}$	···	···	···
HDFN2	31902	189.3127706	+62.2091548	25.4	23.9	24.9	3865.31 ± 0.31	2.17957	1.6 ± 0.2	0.6 ± 0.08	$146.30^{+13.35}_{-12.31}$	···	···	···
	43408	189.4532215	+62.2639356	26.7	25.4	26.3	3886.59 ± 0.47	2.19708	5.6 ± 0.2	2.0 ± 0.1	$72.09^{+6.29}_{-5.89}$	···	···	···
	42659[a]	189.4575590	+62.2917868	25.9	23.8	25.9	3882.07 ± 0.61	2.19336	1.4 ± 0.1	0.51 ± 0.04	$661.41^{132.72}_{-104.76}$	···	···	···
COSMOS3B	38380	149.9205873	+2.3844960	24.4	23.4	24.5	3909.79 ± 0.47	2.21616	6.9 ± 0.7	2.6 ± 0.3	$137.19^{+14.80}_{-13.48}$	2.21256	336 ± 36	0.01
	43982[cd]	149.9766453	+2.4416582	24.3	23.2	24.6	3883.01 ± 0.73	2.19413	6.9 ± 0.6	2.6 ± 0.2	$130.06^{+12.35}_{-11.35}$	2.19333	75 ± 56	0.41
	46597	149.9415665	+2.4688913	24.7	23.8	24.7	3857.99 ± 0.74	2.17355	3.5 ± 0.6	1.2 ± 0.2	$58.75^{+7.07}_{-6.53}$	···	···	···
	38019[a]	149.9020418	+2.3815371	25.9	25.0	25.7	3900.36 ± 0.49	2.2084	1.5 ± 0.2	5.5 ± 0.7	$146.34^{+31.88}_{-26.40}$	···	···	···
	40792[a]	149.9444266	+2.4094991	26.7	25.5	27.4	3901.43 ± 0.53	2.20928	2.3 ± 0.4	0.85 ± 0.14	$394.30^{+121.34}_{-88.39}$	···	···	···
	41547[a]	149.9246216	+2.4166699	26.0	24.9	26.6	3832.08 ± 0.65	2.15224	2.5 ± 0.6	0.86 ± 0.21	$298.88^{+77.85}_{-61.81}$	···	···	···
	44993[a]	149.9744788	+2.4530529	26.5	25.0	26.5	3907.65 ± 0.80	2.2144	2.1 ± 0.4	0.78 ± 0.15	$240.61^{+53.56}_{-43.25}$	···	···	···
HUDF_maB	17001[e]	···	···	···	···	···	3705.44 ± 0.73	2.04806	22.0 ± 4.0	6.7 ± 1.2	···	···	···	···
	31000[e]	···	···	···	···	···	4969.63 ± 0.47	3.08798	3.7 ± 0.6	3.1 ± 0.5	···	···	···	···
SXDS495B	06713	34.4224906	-5.1136338	24.5	23.5	24.6	3894.18 ± 1.02	2.20332	3.9 ± 0.2	1.4 ± 0.1	$118.77^{+5.24}_{-5.04}$	···	···	···
	10600[b]	34.4420541	-5.0486039	23.7	23.0	23.6	3903.62 ± 0.69	2.21109	5.2 ± 0.2	1.9 ± 0.1	$58.19^{+2.62}_{-2.54}$	2.20915	181 ± 53	0.03
	10942	34.4980945	-5.0428800	25.6	24.2	25.6	3887.51 ± 0.55	2.19783	0.77 ± 0.05	0.28 ± 0.02	$134.94^{+9.24}_{-8.68}$	2.19557	212 ± 42	0.12
	10535[a]	34.4246768	-5.0488535	25.9	24.8	26.2	3905.50 ± 0.36	2.21263	3.4 ± 0.2	1.3 ± 0.1	$223.09^{+22.04}_{-19.96}$	···	···	···

NOTE. — Columns: (1) Slit mask. (2) Object ID. (3) Right ascension. (4) Declination. (5)-(7) U, NB387, and B-band magnitudes. (8) Observed wavelength of Lyα measured by the asymmetric gaussian fitting. (9) Redshift of Lyα corrected for the heliocentric motion. (10) Lyα flux uncorrected for slit loss in LRIS spectroscopy. (11) Lyα luminosity. (12) Lyα equivalent width estimated from the NB387 magnitudes. A Lyα position in the transmission curve are taken into account from the spectroscopic redshift of Lyα. (13) Redshift of nebular emission lines corrected for the heliocentric motion (K. Nakajima et al. in preparation.). (14) Lyα velocity offset relative to nebular emission lines. (15) Ratio of Lyα flux in the bluer side relative to the systemic redshift to total Lyα flux.

[a] These objects are reduced without the Keck/LRIS public pipeline.

[b] UV continuum-detected LAEs.

[c] AGN-like objects.

[d] These objects have also been observed with Magellan/MagE in Hashimoto et al. (2013).

[e] K. Nakajima et al. in preparation.

[f] Hashimoto et al. (2013) have reported that LAE 13636 has a $\Delta v_{\rm Ly\alpha}$ of 99^{+16}_{-16} km s^{-1}. However, the Hα line profile would have been affected by a residual of a neighboring OH line due to the low spectral resolution of their Keck-II/NIRSPEC observation ($R \sim 1500$), making it difficult to determine accurately the systemic redshift. Our FMOS spectroscopy with $R \sim 2200$ would securely detect nebular emission less affected by OH lines.

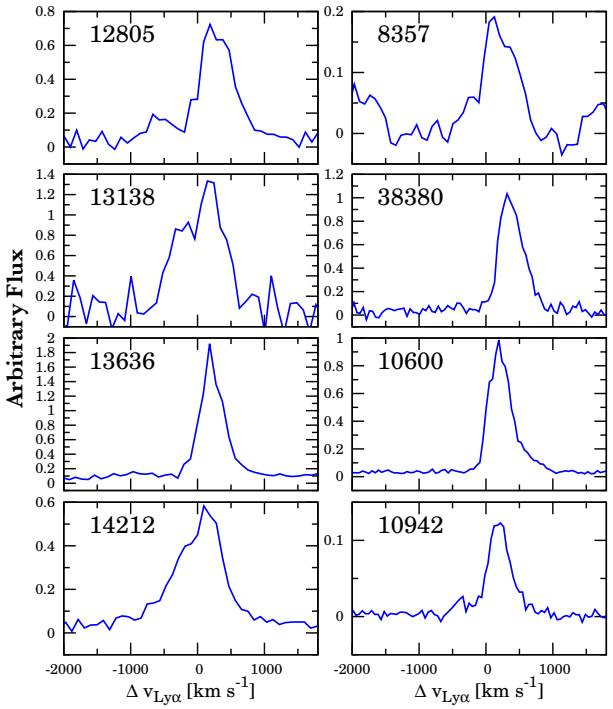

FIG. 4.— Lyα emission lines as a function of velocity for the eight LAEs with detections of nebular lines.

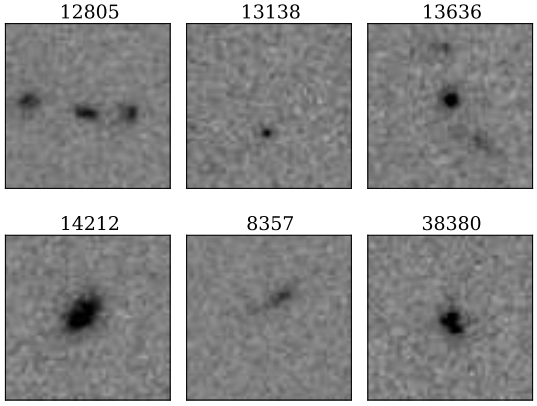

FIG. 5.— *HST* I_{814}-band images of the LAEs with a $z_{\rm sys}$ observed with Keck/LRIS in the COSMOS field. The image size is $2'' \times 2''$. North is up and east is to the left.

The difference in velocity is 30 ± 70 km s^{-1}. The large error in $z_{\rm Ly\alpha}^{\rm LRIS}$ is likely to be due to the lower spectral resolution of LRIS ($R \sim 1000$) than that of MagE ($R \sim 4100$).

Figure 5 shows the *HST*/ACS I_{814}-band images of LAEs with a $z_{\rm sys}$ measurement in the COSMOS field. Unfortunately, the LAEs in the SXDS field are not covered by the CANDELS project. Several LAEs have multiple components, which could be mergers. The merger fraction of LAEs and its Lyα dependence are discussed in Shibuya et al. (2014).

TABLE 3
SUMMARY OF THE LYα-DETECTED OBJECTS IN THE IMACS SPECTROSCOPY

Object	$\lambda_{\rm obs}$ [Å]	$z_{\rm Ly\alpha}$	EW(Lyα) [Å]	$z_{\rm sys}$	$\Delta v_{\rm Ly\alpha}$ [km s^{-1}]
(1)	(2)	(3)	(4)	(5)	(6)
04640	3865.08 ± 0.37	2.17938	$164.75^{+4.63}_{-4.51}$	2.17822	110 ± 138
08204	3895.11 ± 5.59	2.20408	$88.61^{+5.87}_{-5.56}$	2.20329	74 ± 505
09219	3890.71 ± 6.08	2.20047	$29.62^{+2.38}_{-2.29}$	2.20004	40 ± 508
11135	3882.27 ± 0.56	2.19352	$111.96^{+4.78}_{-4.60}$	2.19238	107 ± 151

NOTE. — Columns: (1) Object ID. (2) Observed wavelength of Lyα measured by the asymmetric gaussian fitting. (3) Redshift of Lyα corrected for the heliocentric motion. (4) Lyα equivalent width. (5) Redshift of nebular emission lines corrected for the heliocentric motion (K. Nakajima et al. in preparation.). (6) Velocity offset of Lyα relative to nebular emission lines.

4.3. *Measurement of IS Velocity Offset*

We measure the IS velocity offset of IS absorption lines for our LAEs. Due to the faintness of their UV continuum emission, it is difficult to detect IS absorption lines from high Lyα EW galaxies with $EW \gtrsim 50$ Å in individual spectra. However, owing to the high sensitivity of Keck/LRIS, the rest-frame UV continuum emission is clearly detected from four individual LAEs, LAE 12805, 13636, and 14212 in COSMOS, and LAE 10600 in SXDS, among the 26 Lyα-detected objects.

We first fit a power-law curve to the UV continuum emission in four individual objects in order to normalize the continuum level, and derive the properties of IS absorption lines. The normalized continuum emission in the rest-frame is shown in Figure 6. Next, we fit the symmetric Gaussian profile to each IS absorption line in a wavelength range of ± 5 Å around the expected line center. We summarize the best-fit peak wavelength, line depth, width, and equivalent width in Table 4. The noise in each line is estimated from spectra at $1250 - 1700$ Å avoiding regions close to the absorption lines. Most absorption lines are found to be detected at the $> 5\sigma$ levels except for several LIS lines.

We calculate $\Delta v_{\rm IS}$ in a similar manner as for Lyα in Section 6.1. Several pairs of absorption lines such as O I λ1302-Si II λ1304, and C IV λ1548-C IV λ1550 are likely to be blended at the resolution of our spectroscopy. For this reason, we define the wavelengths of the line pairs as central values between the pairs. We also derive the properties of fine-structure emission lines such as Si II* as summarized in Table 5. We find that the velocity offsets of these ion lines from $z_{\rm sys}$ are almost zero, indicating that the fine-structure emission lines also trace the systemic redshift of galaxies. This is because these emission lines come from nebular regions photoionized by radiation from massive stars (e.g., Shapley et al. 2003).

4.4. *Measurement of HI Covering Fraction*

We estimate the covering fraction, f_c, of surrounding H I gas from the depth of low ionization IS absorption lines for our four continuum-detected LAEs. If the H I gas is distributed in a spherical shell, the depth of the lines may be related to f_c. The covering fraction of any ion is estimated from

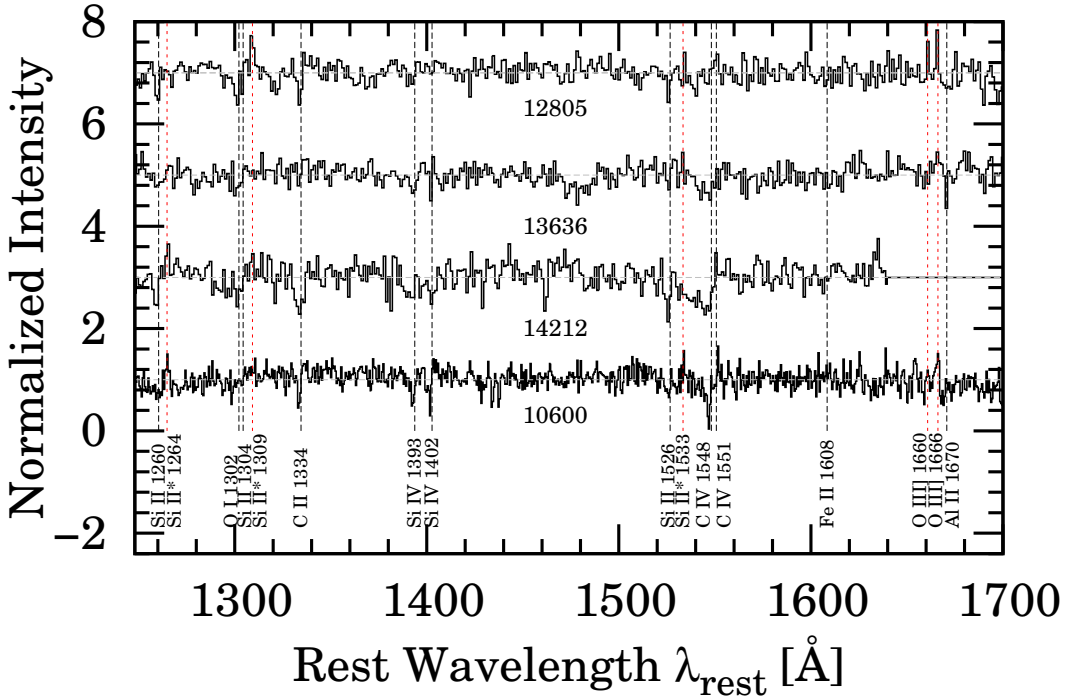

FIG. 6.— Normalized UV spectra of the four continuum detected LAEs. Black and red vertical dashed lines indicates wavelengths of IS absorption and emission lines, respectively.

$$\frac{I}{I_0} = 1 - f_c(1 - e^{-\tau}), \tag{3}$$

where τ, I, and I_0 are optical depth of an absorption line, its residual intensity, and the continuum level, respectively. The optical depth is liked to the column density as

$$\tau = f\lambda\frac{\pi e^2}{m_e c}N = f\lambda\frac{N}{3.768\times10^{14}}, \tag{4}$$

where f, λ, and N are the ion oscillator strength, wavelength of the absorption line in Å, and the column density of the ion in $\mathrm{cm}^{-2}\,(\mathrm{km\ s}^{-1})^{-1}$, respectively. Jones et al. (2013) use Si II λ1260, 1304, and 1526 lines in order to solve the above two equations, and estimate f_c for gravitationally-lensed LBGs at $z \sim 4$. They find best-fit values of N and f_c by fitting observed the Si II line profiles with the intensity as a function of N and f_c, $I(N, f_c)$, derived from the above equations. In addition to the fitting to Si II lines, they use several strong absorption lines, Si II λ1260, O I λ1302, Si II λ1304, C II λ1334, and Si II λ1526 to put a lower limit on f_c via

$$f_c = 1 - \frac{I}{I_0} \tag{5}$$

which is a simplified case of Equation 3 when $\tau \gg 1$. For our LAEs, we estimate f_c in the latter method for the following reasons: (1) it is relatively difficult to fit our Si II line profiles with a low S/N due to the faintness of UV-continuum emission and low resolution of our spectroscopy; and (2) Jones et al. (2013) use mainly the f_c value derived in the latter method in their discussion. We would like to compare f_c for LAEs with that for LBGs in the same manner.

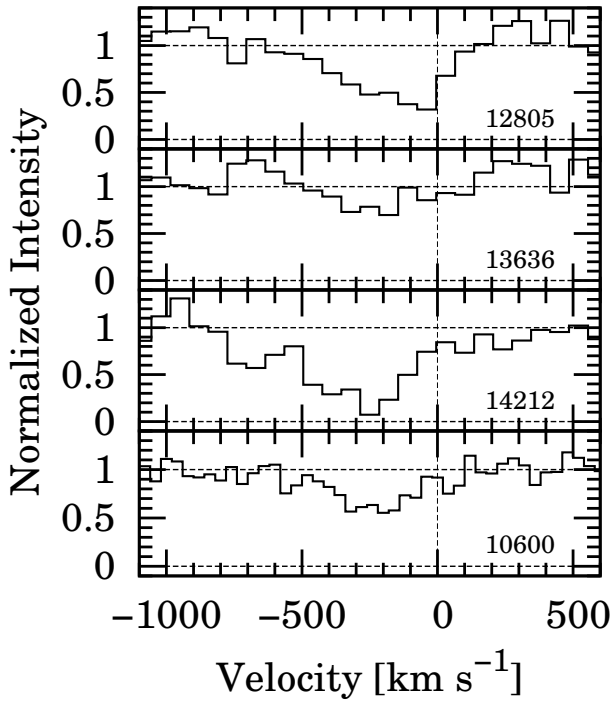

FIG. 7.— Average absorption line profiles of the four continuum-detected LAEs. These profiles are the average of the strong absorption lines, Si II λ1260, C II λ1334, and Si II λ1526 in the same manner as Jones et al. (2013). The transitions of O I λ1302 and Si II λ1304 are not used, since these lines are heavily blended owing to the low spectral resolution.

We derive the average absorption line profile of these

TABLE 4
Absorption Line Features of the UV-continuum Detected LAEs

Object	Ion	$\lambda_{\rm rest}$ [Å]	$\lambda^{\rm sys}_{\rm rest}$ [Å]	I/I_0	σ [Å]	EW(IS) [Å]	$\Delta v_{\rm IS}$ [km s^{-1}]
(1)	(2)	(3)	(4)	(5)	(6)	(7)	(8)
12805	Si II	1260.4221	1259.64 ± 0.43	-0.69 ± 0.56	0.67 ± 0.58	-1.15 ± 0.21	-186 ± 101
EW(Lyα)= 33.73 [Å]	O I	1302.1685	1301.02 ± 0.61	-0.65 ± 0.33	0.97 ± 0.54	-1.56 ± 0.21	$[-518 \pm 139]$
$\Delta v_{{\rm Ly}\alpha} = 258$ [km s^{-1}]	Si II	1304.3702	1301.02 ± 1.52	-0.65 ± 0.33	0.97 ± 0.54	-1.56 ± 0.21	$[-518 \pm 139]$
$m_B = 23.8$	C II	1334.5323	1333.57 ± 0.72	-0.58 ± 0.33	0.90 ± 0.50	-1.32 ± 0.21	-215 ± 162
	Si IV	1393.76018	1392.39 ± 1.40	-0.22 ± 0.27	0.64 ± 0.76	-0.36 ± 0.21	-295 ± 307
	Si II	1526.70698	1525.91 ± 0.36	-0.60 ± 0.17	0.63 ± 0.17	-0.94 ± 0.21	-156 ± 71
	C IV	1548.204	1545.60 ± 1.05	-0.27 ± 0.29	0.70 ± 0.70	-0.48 ± 0.21	$[-750 \pm 203]$
	C IV	1550.781	1545.60 ± 1.05	-0.27 ± 0.29	0.70 ± 0.70	-0.48 ± 0.21	$[-750 \pm 203]$
	Fe II	1608.45085	1607.75 ± 1.11	-0.37 ± 0.48	0.49 ± 0.47	-0.46 ± 0.19	-131 ± 207
	Al II	1670.7886	1670.90 ± 2.13	-0.35 ± 0.37	1.63 ± 1.9	-1.43 ± 0.22	21 ± 382
13636	Si II	1260.4221	1260.23 ± 0.70	-0.21 ± 0.068	1.76 ± 0.65	-0.91 ± 0.19	-46 ± 165
EW(Lyα) = 86.80 [Å]	O I	1302.1685	1301.25 ± 1.20	-0.33 ± 0.26	1.26 ± 1.07	-1.05 ± 0.19	$[-465 \pm 280]$
$\Delta v_{{\rm Ly}\alpha} = 197$ [km s^{-1}]	Si II	1304.3702	1301.25 ± 1.20	-0.33 ± 0.26	1.26 ± 1.07	-1.05 ± 0.19	$[-465 \pm 280]$
$m_B = 24.1$	Si IV	1393.76018	1392.80 ± 0.64	-0.38 ± 0.15	1.27 ± 0.56	-1.19 ± 0.19	-206 ± 138
	Si IV	1402.77291	1401.92 ± 0.62	-0.50 ± 0.74	0.35 ± 0.95	-0.44 ± 0.20	-182 ± 134
	C IV	1548.204	1546.80 ± 0.83	-0.42 ± 0.14	2.00 ± 0.85	-2.09 ± 0.19	$[-518 \pm 161]$
	C IV	1550.781	1546.80 ± 0.83	-0.42 ± 0.14	2.00 ± 0.85	-2.09 ± 0.19	$[-518 \pm 161]$
	Al II	1670.7886	1670.35 ± 0.62	-0.73 ± 0.62	0.39 ± 0.36	-0.71 ± 0.20	-96 ± 112
14212	Si II	1260.4221	1258.98 ± 0.56	-0.65 ± 0.31	0.93 ± 0.48	-1.52 ± 0.24	-343 ± 133
EW(Lyα)= 54.98 [Å]	O I	1302.1685	1301.56 ± 0.74	-0.52 ± 0.28	1.06 ± 0.62	-1.37 ± 0.25	$[-394 \pm 172]$
$\Delta v_{{\rm Ly}\alpha} = 188$ [km s^{-1}]	Si II	1304.3702	1301.56 ± 0.74	-0.52 ± 0.28	1.06 ± 0.62	-1.37 ± 0.25	$[-394 \pm 172]$
$m_B = 24.0$	C II	1334.5323	1333.42 ± 0.55	-0.69 ± 0.16	1.93 ± 0.55	-3.34 ± 0.24	-249 ± 123
	Si IV	1402.77291	1402.54 ± 0.49	-0.49 ± 0.15	1.30 ± 0.43	-1.59 ± 0.24	-50 ± 105
	Si II	1526.70698	1525.49 ± 0.58	-0.86 ± 0.38	0.96 ± 0.42	-2.06 ± 0.24	-238 ± 113
	C IV	1548.204	1545.01 ± 0.60	-0.73 ± 0.17	2.32 ± 0.66	-4.27 ± 0.30	$[-864 \pm 123]$
	C IV	1550.781	1545.01 ± 0.60	-0.73 ± 0.17	2.32 ± 0.66	-4.27 ± 0.30	$[-864 \pm 123]$
	Fe II	1608.45085	1606.52 ± 1.00	-0.32 ± 0.23	0.49 ± 0.40	-0.40 ± 0.25	-360 ± 185
10600	Si II	1260.4221	1258.90 ± 1.07	-0.28 ± 0.11	2.34 ± 1.18	-1.65 ± 0.19	-363 ± 254
EW(Lyα)= 58.19 [Å]	O I	1302.1685	1298.58 ± 0.39	-0.61 ± 0.47	0.28 ± 0.18	-0.42 ± 0.19	$[-1079 \pm 90]^{\rm a}$
$\Delta v_{{\rm Ly}\alpha} = 181$ [km s^{-1}]	Si II	1304.3702	1298.58 ± 0.39	-0.61 ± 0.47	0.28 ± 0.18	-0.42 ± 0.19	$[-1079 \pm 90]^{\rm a}$
$m_B = 23.6$	C II	1334.5323	1333.38 ± 0.45	-0.54 ± 0.28	0.54 ± 0.26	-0.74 ± 0.16	-258 ± 100
	Si IV	1393.76018	1392.57 ± 0.38	-0.50 ± 0.18	0.74 ± 0.26	-0.92 ± 0.16	-256 ± 82
	Si IV	1402.77291	1401.64 ± 0.46	-0.74 ± 0.35	0.32 ± 0.13	-0.60 ± 0.19	-242 ± 97
	Si II	1526.70698	1525.24 ± 0.65	-0.30 ± 0.14	1.00 ± 0.50	-0.75 ± 0.18	-289 ± 127
	C IV	1548.204	1546.75 ± 0.36	-0.92 ± 0.32	0.69 ± 0.22	-1.59 ± 0.19	$[-528 \pm 71]^{\rm b}$
	C IV	1550.781	1546.75 ± 0.36	-0.92 ± 0.32	0.69 ± 0.22	-1.59 ± 0.16	$[-528 \pm 71]^{\rm b}$

Note. — Columns: (1) Object ID. (2) Ion. (3) Wavelength in rest frame. (4) Observed wavelength of the line. (5) Amplitude of the emission line. (6) Width of the absorption line uncorrected for the instrumental broadening. (7) Equivalent width of the line. (8) Velocity offset of emission line relative to nebular emission lines.

[a] The value of Δv assumes that the rest wavelength of the blend is 1303.2694 Å.
[b] The value of Δv assumes that the rest wavelength of the blend is 1549.479 Å.

strong transitions as a function of velocity. In the calculation, we do not use O I λ1302 and Si II λ1304 transitions, since they could be heavily blended owing to the low spectral resolution. The derived average line profiles are shown in Figure 7. The covering fractions are estimated to be ~ 0.7 for LAE 12805, ~ 0.3 for 13636, ~ 0.9 for 14212, and ~ 0.4 for 10600 from the residual intensity in the core of the absorption line profiles. We additionally calculate the average depth of each best-fit Gaussian profile derived in Section 4.3. This alternative is helpful to estimate adequately the depth of a profile with a low S/N. The values of f_c are comparable to those derived from the average line profiles, with the exception of LAE 14212. The difference for LAE 14212 is because the f_c of the average line profile is affected by a singular count of C II λ1334 line profile.

The spectral resolution of our LRIS spectroscopy is ~ 4 times lower than that of Jones et al. (2013), preventing us from making a fair comparison between our LAEs and LBGs. We alternatively estimate EW of strong LIS absorption lines, EW(LIS), for our UV-continuum detected LAEs, and compare with results of composite LBG spectra in Section 6.3.

5. SED FITTING

In order to derive physical properties from stellar components, we perform SED fitting to the eight LAEs with known $z_{\rm sys}$. These LAEs have been imaged in several filters in the COSMOS or SXDS surveys. We use B, V, r, i', and z' data taken with Subaru/Suprime-Cam, J data obtained with UKIRT/WFCAM, K_s data from CFHT/WIRCAM (McCracken et al. 2010), and *Spitzer*/IRAC 3.6, 4.5, 5.8, and 8.0 μm photometry from the Spitzer legacy survey of the UDS field.

The fitting procedure is the same as in Ono et al. (2010). We create a spectral energy distribution (SED) of a starburst galaxy using a stellar population synthesis model, `GALAXEV` (Bruzual & Charlot 2003) including nebular emission (Schaerer & de Barros 2009), with a Salpeter initial mass function with lower and upper mass cutoffs of $m_{\rm L} = 0.1 M_\odot$ and $m_{\rm U} = 100 M_\odot$. We assume a constant star formation history with a metallicity of $Z/Z_\odot = 0.2$. We use Calzetti's law (Calzetti et al. 2000) for the stellar continuum extinction $E(B-V)$. These

TABLE 5
EMISSION LINE FEATURES OF UV-CONTINUUM DETECTED LAEs

Object	Ion	$\lambda_{\rm rest}$ [Å]	$\lambda^{\rm sys}_{\rm rest}$ [Å]	I/I_0	σ [Å]	EW [Å]	$\Delta v_{\rm IS}$ [km s^{-1}]
(1)	(2)	(3)	(4)	(5)	(6)	(7)	(8)
12805	Si II*	1309.276	1309.26 ± 0.44	0.78 ± 0.37	0.82 ± 0.45	1.59 ± 0.21	5 ± 100
	O III]	1660.809	1660.58 ± 0.51	0.64 ± 0.49	0.41 ± 0.31	0.66 ± 0.19	-42 ± 93
	O III]	1666.150	1665.34 ± 0.45	0.89 ± 0.76	0.46 ± 0.29	1.02 ± 0.19	-147 ± 81
13636	Si II*	1533.431	1532.97 ± 0.62	0.48 ± 0.40	0.44 ± 0.39	0.52 ± 0.20	-90 ± 121
	O III]	1666.150	1665.92 ± 1.4	0.39 ± 0.30	1.47 ± 1.23	1.45 ± 0.19	-42 ± 257
14212	Si II*	1264.738	1265.06 ± 0.49	0.80 ± 0.54	0.65 ± 0.45	1.30 ± 0.24	76 ± 117
10600	Si II*	1264.738	1264.94 ± 0.61	0.45 ± 0.32	0.52 ± 0.34	0.59 ± 0.16	47 ± 144
	Si II*	1533.431	1534.03 ± 0.44	0.73 ± 0.48	0.22 ± 0.13	0.41 ± 0.18	116 ± 85
	O III]	1666.150	1665.52 ± 0.97	0.37 ± 0.27	0.94 ± 0.69	0.86 ± 0.20	-113 ± 175

NOTE. — Columns: (1) Object ID. (2) Ion. (3) Wavelength in rest frame. (4) Observed wavelength of the line. (5) Amplitude of the emission line. (6) Width of the absorption line. (7) Equivalent width of the line. (8) Velocity offset of emission line relative to nebular emission lines.

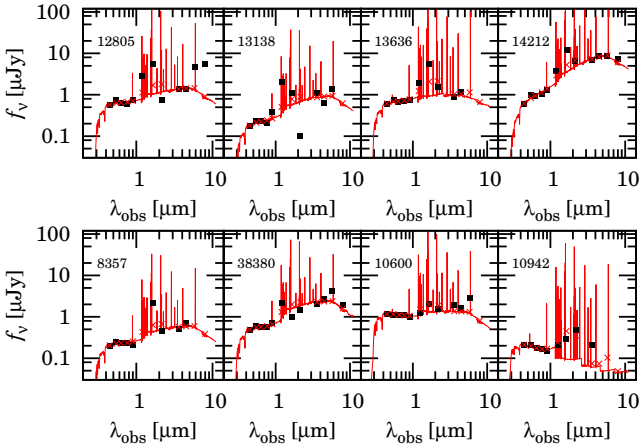

FIG. 8.— Results of SED fitting for the eight LAEs with a $\Delta v_{{\rm Ly}\alpha}$ measurement. Red lines indicate the best-fit model spectra. Black filled squares represent observed magnitudes. Red crosses denote the flux densities at individual filters expected from the best-fit model spectra.

parameters are selected to be the same as those used in Hashimoto et al. (2013) for consistency. The IGM absorption is applied to the spectra using the model of Madau (1995). The best-fit parameters and model spectra are shown in Table 6 and Figure 8, respectively. The best-fit stellar mass of our LAEs ranges from $\log M_* \sim 9$ to ~ 10 which is broadly comparable to that of LBGs. This is because we choose bright objects from our LAE sample for the spectroscopic observations. Thus, the small $\Delta v_{{\rm Ly}\alpha}$ of LAEs does not appear to be caused by a difference in stellar mass between LAEs and LBGs.

6. RESULTS

6.1. *Difference in $\Delta v_{{\rm Ly}\alpha}$ between LAEs and LBGs*

In this section, we investigate statistically the difference in $\Delta v_{{\rm Ly}\alpha}$ between LAEs and LBGs in a compilation of LAEs with a $\Delta v_{{\rm Ly}\alpha}$ measurement in the previous studies including our 12 LAEs. The Lyα velocity offsets have previously been estimated for two objects in McLinden et al. (2011), three in the HETDEX survey (Finkelstein et al. 2011; Chonis et al. 2013), four from (Hashimoto et al. 2013), and two LAEs in the MUSYC project (Guaita et al. 2013) at $z \sim 2-3$. Among

TABLE 6
SED FITTING RESULTS FOR LAEs WITH A SYSTEMIC REDSHIFT

Slit Mask	Object	SFR [$M_\odot$ yr^{-1}]	$E(B-V)$	$\log M_*$ [$M_\odot$]	χ^2_r
(1)	(2)	(3)	(4)	(5)	(6)
COSMOS	12805	$34.7^{+1.3}_{-1.3}$	$0.158^{+0.018}_{-0.018}$	$9.442^{+0.134}_{-0.166}$	6.6
	13138	$12.8^{+1.5}_{-1.6}$	$0.185^{+0.035}_{-0.044}$	$9.483^{+0.218}_{-0.197}$	1.7
	13636	$67.9^{+1.2}_{-1.3}$	$0.185^{+0}_{-0.009}$	$9.051^{+0.115}_{-0.139}$	3.3
	14212	$187.3^{+1.0}_{-1.1}$	$0.326^{+0}_{-0.009}$	$10.364^{+0.048}_{-0}$	13
	08357	$9.52^{+2.1}_{-1.8}$	$0.141^{+0.053}_{-0.053}$	$9.213^{+0.277}_{-0.404}$	0.6
COSMOS3B	38380	$19.8^{+1.2}_{-1.1}$	$0.132^{+0.018}_{-0.009}$	$10.055^{+0.057}_{-0.111}$	1.4
SXDS495B	10600	$23.6^{+1.0}_{-1.1}$	$0.053^{+0}_{-0.009}$	$9.464^{+0.049}_{-0.041}$	4.7
	10942	$14.9^{+33.5}_{-2.3}$	$0.044^{+0.018}_{-0.018}$	$7.734^{+0.110}_{-0.078}$	0.4

NOTE. — Columns: (1) Slit mask. (2) Object ID. (3) SFR. (4) Dust extinction. (5) Stellar mass. (6) Reduced χ^2 of the SED fitting.

the objects in previous studies, COSMOS 13636 from (Hashimoto et al. 2013) is included in our sample of the 12 LAEs. We combine these 11 LAEs with our new 11, and construct a large sample consisting of 22 objects, which doubles the number of LAEs with $\Delta v_{{\rm Ly}\alpha}$ measurements. Figure 9 shows the histogram of $\Delta v_{{\rm Ly}\alpha}$ using the newly-enlarged sample. This is the updated version of Figure 6 in Hashimoto et al. (2013). Similar to Hashimoto et al. (2013), we confirm that $\Delta v_{{\rm Ly}\alpha}$ of LAEs is systematically smaller than the values of LBGs. We carry out the non-parametric Kolmogorv-Smirnov test for the two populations. The K-S probability is calculated to be $\sim 10^{-7}$, indicating that $\Delta v_{{\rm Ly}\alpha}$ is definitively different between LBGs and LAEs. The weighted mean of the 22 objects is $\Delta v_{{\rm Ly}\alpha} = 234 \pm 9$ km s^{-1}.

We plot EW(Lyα) and $\Delta v_{{\rm Ly}\alpha}$ of our new sample in the right panel of Figure 10. We confirm the anti-correlation between EW(Lyα) and $\Delta v_{{\rm Ly}\alpha}$ in high-z star-forming galaxies including objects with a high Lyα EW (*Hashimoto relation*) suggested by Hashimoto et al. (2013). The larger sample clarifies that $\Delta v_{{\rm Ly}\alpha}$ decreases with increasing EW(Lyα). The similar trend has been found for UV-continuum selected galaxies at $z \sim 2-3$. Shapley et al. (2003) have calculated velocity offsets between Lyα emission and IS absorption ($\Delta v_{\rm em-abs}$) for composite spectra of LBGs, and have investigated relation between Lyα EW and $\Delta v_{\rm em-abs}$. Four LBG sub-

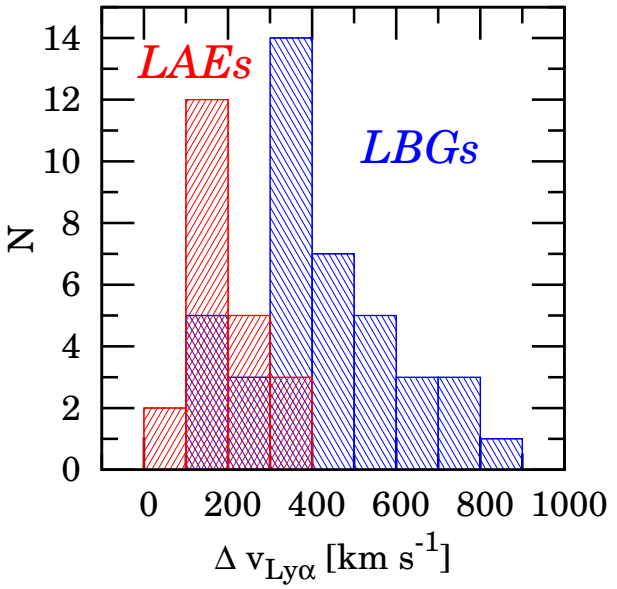

FIG. 9.— Histograms of Lyα velocity offset for the 22 LAEs in this study and literatures (McLinden et al. 2011; Finkelstein et al. 2011; Hashimoto et al. 2013; Guaita et al. 2013; Chonis et al. 2013), and 41 LBGs given by Steidel et al. (2010).

samples divided according to their Lyα EW reveal a trend that Lyα EW increases with decreasing $\Delta v_{\rm em-abs}$ in the EW range of $-15-+50$ Å. The $\Delta v_{\rm em-abs}$ of our UV-continuum detected LAEs is very consistent with the trend of Shapley et al. (2003), as shown in the top panel of Figure 11. Nevertheless, Lyα and IS velocity offsets from $z_{\rm sys}$ would be capable of distinguishing effects of Lyα resonant scattering and galactic outflow on $\Delta v_{\rm em-abs}$.

6.2. *Difference in $\Delta v_{\rm IS}$ between LAEs and LBGs*

We additionally examine a possible difference in $\Delta v_{\rm IS}$ between LAEs and LBGs. The weighted means of $\Delta v_{\rm IS}$ of the absorption lines are calculated to be -134 ± 67, -261 ± 48, -216 ± 56, and -169 ± 52 km s^{-1} for LAE 13636, 10600, 14212, and 12805, respectively. In the calculation of average $\Delta v_{\rm IS}$ for each object, we exclude several line-pairs with a large $\Delta v_{\rm IS}$ of $\lesssim -500$ km s^{-1} which are not reliably determined due to a line blending. As shown in Table 4, we find that almost all IS absorption lines are blueshifted with respect to $z_{\rm sys}$ by $\lesssim -200$ km s^{-1}, which indicates that gaseous outflows are present in the continuum-detected LAEs.

The left panel in Fig. 10 represents the relation between EW(Lyα) and $\Delta v_{\rm IS}$. The average of the four is $\Delta v_{\rm IS}=-204\pm27$ km s^{-1}, which is comparable to that of LBGs (e.g., Erb et al. 2006b; Steidel et al. 2010) in contrast to $\Delta v_{\rm Ly\alpha}$, although the current small sample of LAEs with a $\Delta v_{\rm IS}$ is insufficient to provide a definitive conclusion on $\Delta v_{\rm IS}$ of LAEs and LBGs.

6.3. *Difference in f_c between LAEs and LBGs*

We compare the H I covering fraction f_c of LAEs derived in Section 4.4 with that of $z\sim2-3$ LBGs in Jones et al. (2013). Note that we here place lower limits on f_c when $\tau\gg1$. Figure 12 displays the relation between f_c and Lyα EW, indicating a tentative trend that f_c decreases with Lyα EW. This trend has already been found in Jones et al. (2013) using an LBG sample. We find that the trend continues into objects with a higher Lyα EW. Our slope of the trend is slightly steeper than that in Jones et al. (2013), which would result from the wider dynamic range in Lyα EW. However, this trend could arise from the difference in the spectral resolution, although this tendency may marginally be found for LAEs alone. In addition to f_c, we compare EW(LIS) between LAEs and $z=3-4$ LBGs in the bottom panel of Figure 11. Shapley et al. (2003) have found that EW(LIS) decreases with increasing EW(Lyα) with composite spectra of LBGs. Our LAEs with EW(Lyα) $=30-90$ Å follow the trend between EW(Lyα) and EW(LIS), which might be indicative of a low velocity dispersion and/or low f_c, as suggested by Shapley et al. (2003). These results related to the low f_c imply the need for modeling Lyα line profiles emitted from a non-spherical shell of neutral gas (e.g., Zheng & Wallace 2013; Behrens et al. 2014).

7. DISCUSSION

7.1. *Origin of Small $\Delta v_{\rm Ly\alpha}$ in LAEs*

As described in the previous sections, we definitely confirm the anti-correlation between $\Delta v_{\rm Ly\alpha}$ and Lyα EW by using a larger LAE sample than previously available. In this section, we explore the physical origin of the small $\Delta v_{\rm Ly\alpha}$ in high Lyα EW galaxies.

Models predict that the redshift of the Lya emission line should increase with either outflow velocity or neutral hydrogen column density ($N_{\rm HI}$) (Verhamme et al. 2006, 2008). We have shown that the outflow velocities of LAE are comparable to those of LBGs, so the smaller $\Delta v_{\rm Ly\alpha}$ for LAE is likely to be due to lower column densities in these objects.

In order to address the origin of the small $\Delta v_{\rm Ly\alpha}$ in LAEs, we introduce the *velocity offset ratio*,

$$R_{\rm IS}^{\rm Ly\alpha}\equiv\frac{\Delta v_{\rm Ly\alpha}}{\Delta v_{\rm IS}}. \quad (6)$$

The value of $R_{\rm IS}^{\rm Ly\alpha}$ could trace purely physical properties such as $N_{\rm HI}$ and the dust amount by excluding the kinematic effect of a bulk outflow, since the quantity is normalized by the outflowing velocity, as suggested in (Verhamme et al. 2006). Hashimoto et al. (2013) infer the average value of $\Delta v_{\rm IS}$ for LAEs from a stacked spectrum of four LAEs with a $z_{\rm sys}$, and compare $R_{\rm IS}^{\rm Ly\alpha}$ between LAEs and LBGs. In the stacking analysis, $R_{\rm IS}^{\rm Ly\alpha}$ is found to be ~1 for LAEs which is slightly-smaller than that of LBGs, but the uncertainties are large.

Here, we estimate $R_{\rm IS}^{\rm Ly\alpha}$ for the four continuum-detected LAEs, and compare the quantities with those of $z=2-3$ LBGs in Erb et al. (2006a,b). In the comparison, we use LBGs with a negative $\Delta v_{\rm IS}$ value that indicates the outflow is present. The LAEs have a $R_{\rm IS}^{\rm Ly\alpha}$ of $\sim0.6-1.4$, while LBGs have a wide variety of the quantity from 0 to ~10. Nevertheless, the average $R_{\rm IS}^{\rm Ly\alpha}$ for the LAEs is systematically smaller than that of LBGs. This indicates that LAEs tend to have a small $N_{\rm HI}$ compared to LBGs based on the expanding gas shell model of Verhamme et al. (2006). The small $R_{\rm IS}^{\rm Ly\alpha}$ in LAEs would

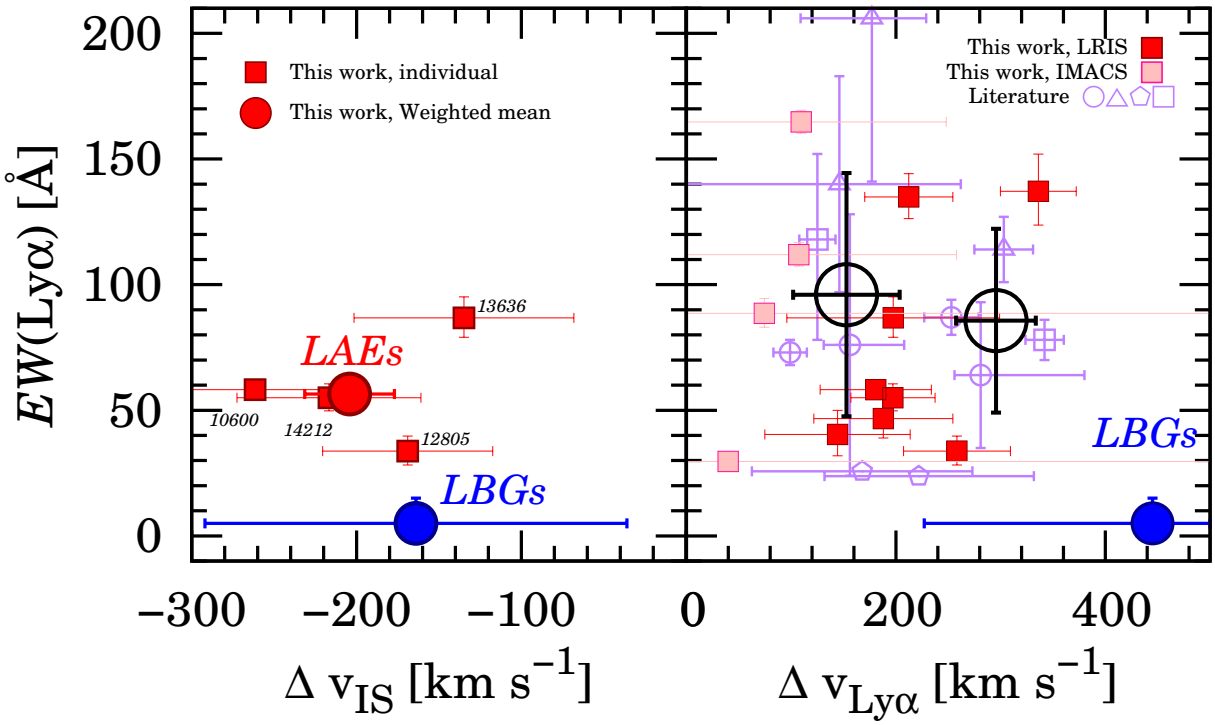

FIG. 10.— Rest-frame Lyα EW as a function of $\Delta v_{\rm Ly\alpha}$ (right) and $\Delta v_{\rm IS}$ (left). The red and magenta squares indicates LAEs observed with Keck/LRIS and Magellan/IMACS, respectively. The purple open symbols denote LAEs in the previous studies, (squares; McLinden et al. 2011), (triangles; Finkelstein et al. 2011; Chonis et al. 2013), (circles; Hashimoto et al. 2013), and (pentagons; Guaita et al. 2013). The black open circles with error bars represent the average EW in each $\Delta v_{\rm Ly\alpha}$ bin. The large red circle in the left panel depicts the weighted mean of the four continuum-detected LAEs. The blue symbol denotes the average of 41 LBGs, with the error bars corresponding to the 68 percentiles of the $\Delta v_{\rm Ly\alpha}$ and $\Delta v_{\rm IS}$ distributions (Steidel et al. 2010) and the EW distribution (Reddy et al. 2008).

be indicative of a small $N_{\rm HI}$ in LAEs.

Next, we examine possible correlations of $\Delta v_{\rm Ly\alpha}$ and $R_{\rm IS}^{\rm Ly\alpha}$ with physical properties inferred from the SED fitting (Section 5). In correlation tests, $\Delta v_{\rm Ly\alpha}$ and $R_{\rm IS}^{\rm Ly\alpha}$ correlate most strongly with mass-related quantities, and SFR, respectively. Figures 13 and 14 show the correlations of these quantities, respectively, including LAEs and LBGs with a $z_{\rm sys}$ in the literatures. The SFR value of several LAEs is based on a Hα flux through the relation of Kennicutt (1998). The SFR based on a Hα flux is found to be comparable to the value inferred from SED fitting (Hashimoto et al. 2013). We conduct Spearman rank correlation tests in order to find the most related physical quantities to $\Delta v_{\rm Ly\alpha}$ and $R_{\rm IS}^{\rm Ly\alpha}$ in the same manner as Steidel et al. (2010). Table 8 summarizes the results of the Spearman rank correlation tests.

For Lyα velocity offsets, we find that the $\Delta v_{\rm Ly\alpha}$ strongly correlates with SFR and stellar mass, which has not been observed previously in an LBG sample (Steidel et al. 2010). These correlations may have merged because our sample covers larger dynamic ranges of SFR and M_*. The correlation between $\Delta v_{\rm Ly\alpha}$ and sSFR may arise from the stellar mass.

As far as the velocity offset ratio is concerned, we do not find a notable correlation between $R_{\rm IS}^{\rm Ly\alpha}$ and the physical properties. Nonetheless, the correlation tests indicate that $R_{\rm IS}^{\rm Ly\alpha}$ most correlates with SFR among the four physical quantities. The correlation may reflect the connection between star formation and $N_{\rm HI}$, if $R_{\rm IS}^{\rm Ly\alpha}$ is sensitive to $N_{\rm HI}$. A larger sample of LAEs with a $R_{\rm IS}^{\rm Ly\alpha}$ measurement might reveal its physical connections with galactic properties.

7.2. *What is the Physical Origin of Strong Lyα Emission?*

With our larger sample of LAEs with a $z_{\rm sys}$, we confirm conclusively that LAEs typically have a smaller $\Delta v_{\rm Ly\alpha}$ than LBGs with a lower Lyα EW, while their outflowing velocities are similar in the two populations. These results yield a small $R_{\rm IS}^{\rm Ly\alpha}$ in LAEs, which indicates a small $N_{\rm HI}$ in galaxies with a high Lyα EW. The anti-correlations of f_c and EW(LIS) with Lyα EW in Figures 12 and 11 are consistent with the small $N_{\rm HI}$ in LAEs. The patchy H I gas clouds surrounding the central source would lead to a small flux-averaged $N_{\rm HI}$ corresponding to a small $R_{\rm IS}^{\rm Ly\alpha}$. In this condition, Ly$\alpha$ photons could easily escape less affected by resonant scattering in the clouds. The results of our kinematic analyses support the idea that the H I column density is a key quantity determining Lyα emissivity.

Moreover, recent NIR spectroscopy by Nakajima et al. (2013) has suggested that LAEs have a large [O III]/[O II] ratio, indicating these systems are highly ionized with density-bounded H II regions. This tendency has been confirmed by a subsequent systematic study in Nakajima & Ouchi (2013). The large [O III]/[O II] ratio also indicates a low column density of H I gas. A stacked UV continuum spectrum of our eight LAEs shows that LIS absorption lines have a low EW, as shown in Figures

TABLE 7
Properties of the NB-selected Galaxies with detections of Lyα and Nebular Emission lines in the Previous Studies

Object	$z_{\rm sys}$	EW(Lyα) [Å]	$\Delta v_{\rm Ly\alpha}$ [km s^{-1}]	SFR [$M_\odot$ yr^{-1}]	$E(B-V)$	$\log M_*$ [$M_\odot$]	Comments
(1)	(2)	(3)	(4)	(5)	(6)	(7)	(8)
McLinden et al. (2011)							
LAE27878	3.11879	118^{+34}_{-40}	125 ± 17.3	32^{+9}_{-7}	···	$9.97^{+0.378}_{-0.395}$ [a]	[O III]λ5007
LAE40844	3.11170	78^{+8}_{-8}	342 ± 18.3	113^{+120}_{-60}	···	$9.80^{+0.734}_{-0.363}$ [a]	
Finkelstein et al. (2011) and Chonis et al. (2013)							
HPS 194	2.28628	114 ± 13	303 ± 28	> 29.3 [b]	0.09 ± 0.06	$10.2^{+0.08}_{-0.14}$	HETDEX sample
HPS 256	2.49024	206 ± 65	177^{+52}_{-68}	> 35.4 [b]	0.10 ± 0.09	$8.28^{+0}_{-0.02}$	Hβ, [O III]λ4959, [O III]λ5007, Hα
HPS 251	2.28490	140 ± 43	146^{+116}_{-156}	> 9.9 [b]	0.07 ± 0.08	$9.04^{+0.73}_{-0.04}$	
Hashimoto et al. (2013)							
CDFS-3865	2.17210	64^{+29}_{-29}	281^{+99}_{-25}	190^{+13}_{-13} [b]	$0.185^{+0.009}_{-0.009}$	$9.50^{+0.028}_{-0.018}$	Subaru NB387 sample
CDFS-6482	2.20443	76^{+52}_{-52}	156^{+52}_{-25}	48^{+10}_{-9} [b]	$0.185^{+0.026}_{-0.018}$	$9.72^{+0.087}_{-0.071}$	[O III]λ5007, Hα
COSMOS-13636	2.16125[c]	73^{+5}_{-5}	99^{+16}_{-16} [c]	18^{+3}_{-3} [b]	$0.273^{+0.018}_{-0.079}$	$9.30^{+0.078}_{-0.330}$	
COSMOS-30679	2.19776	87^{+7}_{-7}	253^{+26}_{-26}	45^{+5}_{-5} [b]	$0.528^{+0.026}_{-0.026}$	$10.3^{+0.124}_{-0.151}$	
Guaita et al. (2013)							
LAE27	3.0830	25.7	167.8 ± 105.3	···	$\lesssim 0.1$	$9.95^{+0.13}_{-0.17}$	MUSYC sample
z3LAE2	3.1118	23.8	221.8 ± 90.0	···	$0.32^{+0.06}_{-0.23}$	$9.95^{+0.13}_{-0.17}$	Hβ, [O III]λ4959, [O III]λ5007

Note. — Columns: (1) Object ID. (2) Systemic redshift. (3) Lyα equivalent width. (4) Lyα velocity offset. (5) SFR. (6) Dust extinction. (7) Stellar mass. (8) Comments.
[a] Estimated in Rhoads et al. (2014).
[b] Based on Hα flux.
[c] The $\Delta v_{\rm Ly\alpha}$ of this object is calculated to be 197 ± 102 km s^{-1} in our FMOS observation with higher spectral resolution than that of the Keck-II/NIRSPEC spectrosocpy in Hashimoto et al. (2013) (see Table 2).

TABLE 8
Correlations between Lyα Kinematics and Galaxy Properties

Quantity	$\Delta v_{\rm Ly\alpha}$	$N_{\Delta v_{\rm Ly\alpha}}$	$R_{\rm IS}^{\rm Ly\alpha}$	$N_{R_{\rm IS}^{\rm Ly\alpha}}$
(1)	(2)	(3)	(4)	(5)
SFR	0.065	53	0.241	31
sSFR	−0.098	51	−0.852	31
$E(B-V)$	0.792	54	0.272	34
M_*	0.001	52	0.810	31

Note. — Columns: (1) Physical quantity. (2) Probabilities satisfying the null hypothesis that the quantities are not correlated in Spearman rank correlation tests. A smaller absolute value of the probabilities implies that a physical property more correlates with a Lyα velocity offset. Negative values indicates anti-correlations. (3) Number of galaxies in the correlation test between $\Delta v_{\rm Ly\alpha}$ and physical quantities. (4)-(5) Probabilities and galaxy numbers in the correlation tests for $R_{\rm IS}^{\rm Ly\alpha}$. Two LBGs with an extremely high $R_{\rm IS}^{\rm Ly\alpha}$ value of > 25 are excluded in the correlation tests.

15 (see also Fig. 11). The weak LIS absorption lines are consistent with a large [O III]/[O II] ratio in LAEs (e.g., Jones et al. 2012).

In our first paper of the series investigating LAE structures, we find that LAEs with a high Lyα EW tend to be a non-merger, to show a small Lyα spatial offset between Lyα and stellar continuum emission $\delta_{\rm Ly\alpha}$, and to have a small ellipticity by using a large sample of 426 LAEs (Shibuya et al. 2014). On the basis of these results on the gas distribution, the difference in H I column density explains the Lyα-EW dependences of the merger fraction, the Lyα spatial offset, and the galaxy inclination. For objects with density-bounded H II regions, Lyα photons would directly escape from central ionizing sources, which produce a small $\delta_{\rm Ly\alpha}$. The low H I abundance along the line of sight also induces the preferential escape of Lyα to the face-on direction.

All of the above results suggest that ionized regions with small amounts of H I gas dominate in galaxies with a high Lyα.

8. SUMMARY AND CONCLUSION

We carry out deep optical spectroscopy for our large sample of LAEs at $z = 2.2$ in order to detect their Lyα lines with Keck/LRIS. We compare redshifts of the Lyα and nebular emission lines detected with Subaru/FMOS, and calculate $\Delta v_{\rm Ly\alpha}$ for new 11 LAEs. This observation doubles the sample size of LAEs with a $\Delta v_{\rm Ly\alpha}$ measurement in literatures.

The conclusions of this study are summarized below.

- Almost all of our new LAEs have a $\Delta v_{\rm Ly\alpha}$ of ~ 200 km s^{-1} which is systematically-smaller than that of LBGs. Using 22 LAEs with $\Delta v_{\rm Ly\alpha}$ measurements taken from our new observations and the literature, we definitively confirm the anti-correlation between Lyα EW and $\Delta v_{\rm Ly\alpha}$ suggested by previous work.

- Long exposure times and the high sensitivity of LRIS at blue wavelengths enabled us to successfully detect IS absorption lines against faint UV continua from four individual LAEs. These IS absorption lines are found to be blueshifted from the systemic redshift by $200 - 300$ km s^{-1}, indicating strong gaseous outflows are present even in LAEs.

- We estimate $R_{\rm IS}^{\rm Ly\alpha}$ ($\equiv \Delta v_{\rm Ly\alpha}/\Delta v_{\rm IS}$) that would be a quantity sensitive to $N_{\rm HI}$ for the four UV continuum-detected LAEs. We find the value of

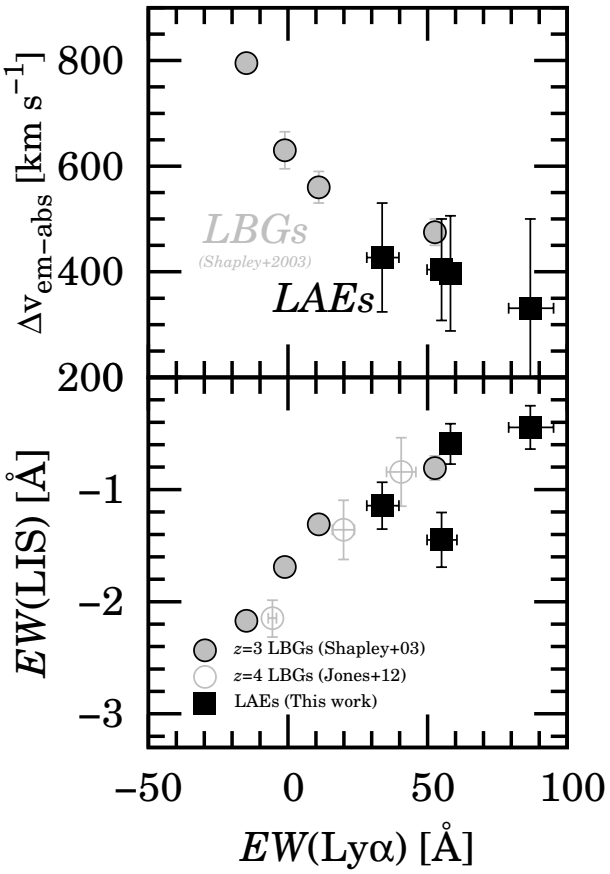

FIG. 11.— Top: velocity offset between Lyα emission and LIS absorption lines as a function of EW(Lyα). Bottom: equivalent width of LIS absorption lines as a function of EW(Lyα). The black filled squares indicate the UV-continuum detected LAEs. The gray open and filled circles denote composite LBG spectra at $z \sim 3$ (Shapley et al. 2003) and $z \sim 4$ (Jones et al. 2012), respectively. The EW(LIS) of LAEs is the average equivalent width of six strong LIS absorption lines, Si II 1260, O I+Si II 1303, C II 1334, Si II 1526, Fe II 1608, and Al II 1670.

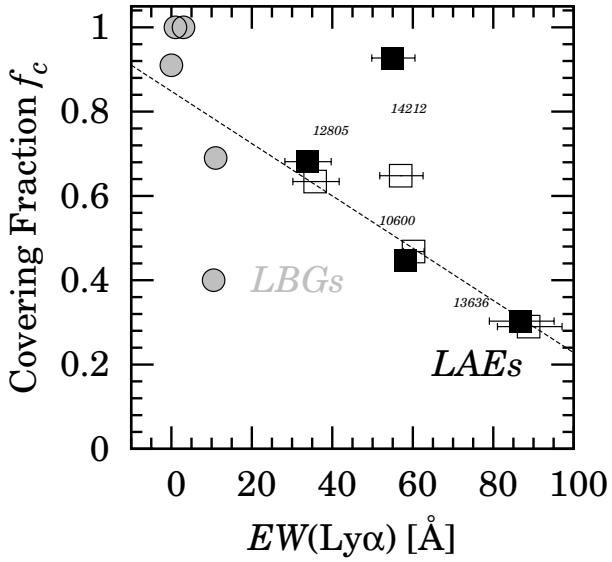

FIG. 12.— Covering fraction of H I gas, f_c, as a function of Lyα EW. The f_c values of the four LAEs are estimated from the depth of the average values in the individual profile-fitting (open squares; Table 4) and average LIS absorption line profiles (filled squares; Fig. 7). The gray circles indicate LBGs at $z = 2-3$ in Jones et al. (2013). The dashed line denotes a linear fit to the data.

$R_{\rm IS}^{{\rm Ly}\alpha}$ in LAEs to be smaller than that of LBGs, indicating a lower $N_{\rm HI}$ in LAEs. We performed a test for correlations between $R_{\rm IS}^{{\rm Ly}\alpha}$ and physical properties inferred from SED fitting. As a result, we tentatively conclude that SFR may be most closely related to $R_{\rm IS}^{{\rm Ly}\alpha}$. The correlation may suggest that the star formation preferentially occurs in systems with large amounts of neutral hydrogen gas, which would have a larger value of $R_{\rm IS}^{{\rm Ly}\alpha}$.

- We estimate the covering fraction, f_c, of surrounding H I gas from the depth of LIS absorption lines the four LAEs. We identify a tentative trend for f_c to decrease with increasing Lyα EW, as suggested by a study for LBGs in Jones et al. (2013). A central source being covered by patchy H I gas clouds would lead to a small flux-averaged $N_{\rm HI}$ corresponding to a small $R_{\rm IS}^{{\rm Ly}\alpha}$. In this condition, Ly$\alpha$ photons could easily escape less affected by resonant scattering in the clouds.

- The results of our kinematic analyses support the idea that the H I column density is a key quantity determining Lyα emissivity.

In this kinematic study, we obtain $\Delta v_{\rm IS}$, $R_{\rm IS}^{{\rm Ly}\alpha}$, and f_c only for objects with a moderate Lyα EW of $20-100$ Å which overlaps with the Lyα EW range of LBG samples in e.g., Shapley et al. (2003). We need to estimate these quantities for objects with a higher Lyα EW in order to check whether such objects follow the kinematic trends found in this study.

We would like to thank Anne Verhamme, Zheng Zheng, Lennox L. Cowie, Esther M. Hu, and James E. Rhoads for useful discussion, and an anonymous referee, Mark Dijkstra, and Lucia Guaita for constructive comments. This paper is based on data collected with the Subaru Telescope, which is operated by the National Astronomical Observatory of Japan. Some of the data presented herein were obtained at the W.M. Keck Observatory, which is operated as a scientific partnership among the California Institute of Technology, the University of California and the National Aeronautics and Space Administration. The Observatory was made possible by the generous financial support of the W.M. Keck Foundation. The reduction pipeline used to reduce the LRIS data was developed at UC Berkeley with support from NSF grant AST-0071048. This work is based on observations taken by the CANDELS Multi-Cycle Treasury Program with the NASA/ESA *HST*, which is operated by the Association of Universities for Research in Astronomy, Inc., under NASA contract NAS5-26555. The NB387 data used in this work were collected at the Subaru Telescope, which is operated by the National Astronomical Observatory of Japan. This work is based in part on observations made with the *Spitzer Space Telescope*, which is operated by the Jet Propulsion Laboratory, California Institute of Technology under a contract with NASA.

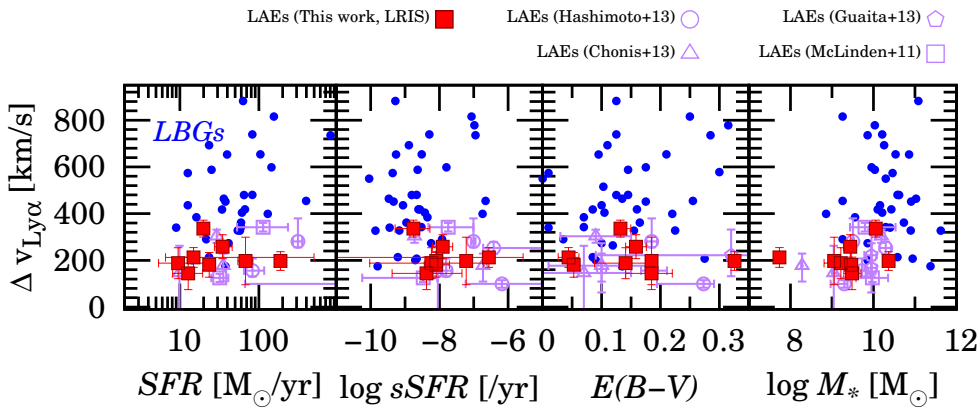

FIG. 13.— Correlations between $\Delta v_{\rm Ly\alpha}$ and physical properties inferred from the SED fitting. The symbols are the same as Figure 10. We multiply the physical quantities of LBGs in Erb et al. (2006a) by 1.8, because they use a Chabrier IMF (Chabrier 2003) in the SED fitting.

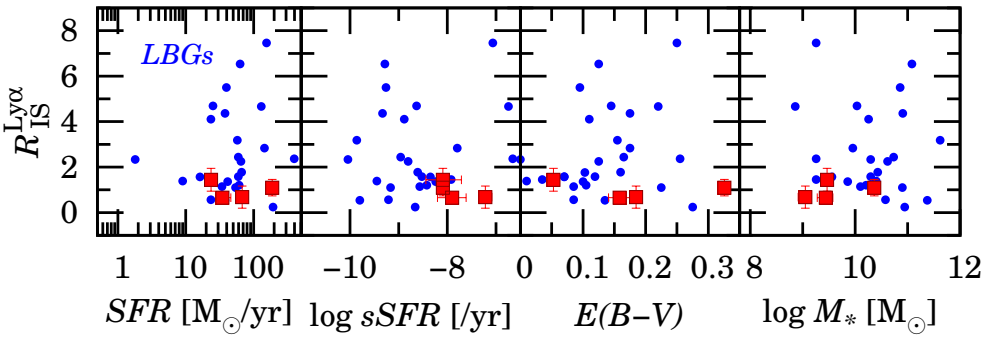

FIG. 14.— Same as Figure 13, but for $R_{\rm IS}^{\rm Ly\alpha}$. Red squares indicate the four UV continuum-detected LAEs.

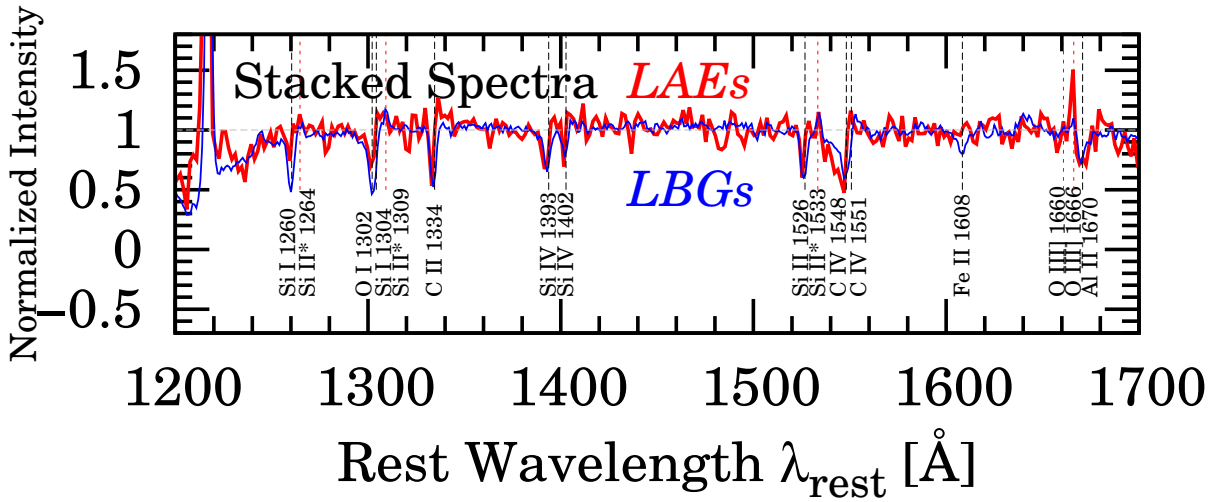

FIG. 15.— Composite rest-frame UV spectra of the eight LAEs observed with Keck/LRIS (red) and LBGs in Shapley et al. (2003) (blue). The spectra are normalized to unity in the continuum levels. Black and red vertical dashed lines indicates wavelengths of IS absorption and emission lines, respectively.

Support for this work was provided by NASA through an award issued by JPL/Caltech. This work was supported by World Premier International Research Center Initiative (WPI Initiative), MEXT, Japan. This work was supported by KAKENHI (23244025) and (21244013) Grant-in-Aid for Scientific Research (A) through Japan Society for the Promotion of Science (JSPS). MR was supported by NSF grant AST-1108815.

Facilities: Subaru (Suprime-Cam, FMOS), Keck:I (LRIS), Magellan:Baade (IMACS).

REFERENCES

Behrens, C., Dijkstra, M., & Niemeyer, J. C. 2014, A&A, 563, A77

Bruzual, G., & Charlot, S. 2003, MNRAS, 344, 1000

Calzetti, D., Armus, L., Bohlin, R. C., Kinney, A. L., Koornneef, J., & Storchi-Bergmann, T. 2000, ApJ, 533, 682
Chabrier, G. 2003, PASP, 115, 763
Chonis, T. S., et al. 2013, ApJ, 775, 99
Christensen, L., et al. 2012, MNRAS, 427, 1973
Ciardullo, R., et al. 2012, ApJ, 744, 110
Cowie, L. L., Barger, A. J., & Hu, E. M. 2010, ApJ, 711, 928
Dijkstra, M., & Kramer, R. 2012, MNRAS, 424, 1672
Dijkstra, M., & Wyithe, J. S. B. 2010, MNRAS, 408, 352
Dressler, A., Martin, C. L., Henry, A., Sawicki, M., & McCarthy, P. 2011, ApJ, 740, 71
Duval, F., Schaerer, D., Östlin, G., & Laursen, P. 2013, ArXiv e-prints
Erb, D. K., Pettini, M., Shapley, A. E., Steidel, C. C., Law, D. R., & Reddy, N. A. 2010, ApJ, 719, 1168
Erb, D. K., Steidel, C. C., Shapley, A. E., Pettini, M., Reddy, N. A., & Adelberger, K. L. 2006a, ApJ, 647, 128
—. 2006b, ApJ, 646, 107
Finkelstein, S. L., Rhoads, J. E., Malhotra, S., Grogin, N., & Wang, J. 2008, ApJ, 678, 655
Finkelstein, S. L., Rhoads, J. E., Malhotra, S., Pirzkal, N., & Wang, J. 2007, ApJ, 660, 1023
Finkelstein, S. L., et al. 2011, ApJ, 729, 140
Furusawa, H., et al. 2008, ApJS, 176, 1
Gawiser, E., et al. 2007, ApJ, 671, 278
Giacconi, R., et al. 2001, ApJ, 551, 624
Giavalisco, M., et al. 2004, ApJ, 600, L93
Gronwall, C., Bond, N. A., Ciardullo, R., Gawiser, E., Altmann, M., Blanc, G. A., & Feldmeier, J. J. 2011, ApJ, 743, 9
Gronwall, C., et al. 2007, ApJ, 667, 79
Guaita, L., Francke, H., Gawiser, E., Bauer, F. E., Hayes, M., Östlin, G., & Padilla, N. 2013, A&A, 551, A93
Guaita, L., et al. 2011, ApJ, 733, 114
Hashimoto, T., Ouchi, M., Shimasaku, K., Ono, Y., Nakajima, K., Rauch, M., Lee, J., & Okamura, S. 2013, ApJ, 765, 70
Hu, E. M., Cowie, L. L., Barger, A. J., Capak, P., Kakazu, Y., & Trouille, L. 2010, ApJ, 725, 394
Jones, T., Stark, D. P., & Ellis, R. S. 2012, ApJ, 751, 51
Jones, T. A., Ellis, R. S., Schenker, M. A., & Stark, D. P. 2013, ApJ, 779, 52
Kashikawa, N., et al. 2006, ApJ, 648, 7
—. 2011, ApJ, 734, 119
Kennicutt, Jr., R. C. 1998, ARA&A, 36, 189
Kimura, M., et al. 2010, PASJ, 62, 1135
Komatsu, E., et al. 2011, ApJS, 192, 18
Kulas, K. R., Shapley, A. E., Kollmeier, J. A., Zheng, Z., Steidel, C. C., & Hainline, K. N. 2012, ApJ, 745, 33
Laursen, P., Duval, F., & Östlin, G. 2013, ApJ, 766, 124
Laursen, P., & Sommer-Larsen, J. 2007, ApJ, 657, L69
Laursen, P., Sommer-Larsen, J., & Andersen, A. C. 2009, ApJ, 704, 1640
Madau, P. 1995, ApJ, 441, 18
McCracken, H. J., et al. 2010, ApJ, 708, 202
McLinden, E. M., et al. 2011, ApJ, 730, 136
Miyazaki, S., et al. 2002, PASJ, 54, 833
Momose, R., et al. 2014, ArXiv e-prints
Nakajima, K., & Ouchi, M. 2013, ArXiv e-prints
Nakajima, K., Ouchi, M., Shimasaku, K., Hashimoto, T., Ono, Y., & Lee, J. C. 2013, ApJ, 769, 3
Nakajima, K., et al. 2012, ApJ, 745, 12
Neufeld, D. A. 1991, ApJ, 370, L85
Oke, J. B., & Gunn, J. E. 1983, ApJ, 266, 713
Oke, J. B., et al. 1995, PASP, 107, 375
Ono, Y., et al. 2010, MNRAS, 402, 1580
Ota, K., et al. 2008, ApJ, 677, 12
Ouchi, M., et al. 2008, ApJS, 176, 301
—. 2010, ApJ, 723, 869
Pettini, M., Shapley, A. E., Steidel, C. C., Cuby, J.-G., Dickinson, M., Moorwood, A. F. M., Adelberger, K. L., & Giavalisco, M. 2001, ApJ, 554, 981
Rauch, M., et al. 2008, ApJ, 681, 856
Reddy, N. A., Steidel, C. C., Pettini, M., Adelberger, K. L., Shapley, A. E., Erb, D. K., & Dickinson, M. 2008, ApJS, 175, 48
Rhoads, J. E., Malhotra, S., Richardson, M. L. A., Finkelstein, S. L., Fynbo, J. P. U., McLinden, E. M., & Tilvi, V. S. 2014, ApJ, 780, 20
Schaerer, D., & de Barros, S. 2009, A&A, 502, 423
Schenker, M. A., Ellis, R. S., Konidaris, N. P., & Stark, D. P. 2013, ApJ, 777, 67
Scoville, N., et al. 2007, ApJS, 172, 1
Shapley, A. E., Steidel, C. C., Pettini, M., & Adelberger, K. L. 2003, ApJ, 588, 65
Shibuya, T., Kashikawa, N., Ota, K., Iye, M., Ouchi, M., Furusawa, H., Shimasaku, K., & Hattori, T. 2012, ApJ, 752, 114
Shibuya, T., Ouchi, M., Nakajima, K., Yuma, S., Hashimoto, T., Shimasaku, K., Mori, M., & Umemura, M. 2014, ApJ, 785, 64
Steidel, C. C., Adelberger, K. L., Shapley, A. E., Pettini, M., Dickinson, M., & Giavalisco, M. 2000, ApJ, 532, 170
Steidel, C. C., Erb, D. K., Shapley, A. E., Pettini, M., Reddy, N., Bogosavljević, M., Rudie, G. C., & Rakic, O. 2010, ApJ, 717, 289
Steidel, C. C., Shapley, A. E., Pettini, M., Adelberger, K. L., Erb, D. K., Reddy, N. A., & Hunt, M. P. 2004, ApJ, 604, 534
Verhamme, A., Schaerer, D., Atek, H., & Tapken, C. 2008, A&A, 491, 89
Verhamme, A., Schaerer, D., & Maselli, A. 2006, A&A, 460, 397
Yajima, H., Li, Y., Zhu, Q., Abel, T., Gronwall, C., & Ciardullo, R. 2012, ArXiv e-prints
Zheng, Z., Cen, R., Trac, H., & Miralda-Escudé, J. 2010, ApJ, 716, 574
Zheng, Z., & Wallace, J. 2013, ArXiv e-prints